The impact of slantwise descending dry intrusions on the marine boundary layer and air-sea interface over the ARM Eastern North Atlantic site

E. Ilotoviz [1], V. P. Ghate [2], S. Raveh-Rubin[1]

[1] Department of Earth and Planetary Sciences, Weizmann Institute of Science, Rehovot, Israel

[2] Argonne National Laboratory, Lemont, USA

December, 2020

Submitted to Journal of Geophysical Research-Atmospheres

Corresponding author address:

Ilotoviz Eyal

Email: eyal.ilotoviz@weizmann.ac.il

Abstract

Dry intrusions (DIs) are synoptic-scale slantwise descending airstreams from the midlatitude upper troposphere towards the boundary layer at lower latitudes. Typically occurring behind cold fronts, such intrusions of dry air often reach the boundary layer and cause its deepening, thereby affecting boundary-layer clouds. Although subsidence is generally an inherent feature of the subtropical marine boundary layer (MBL), it is unclear how the MBL reacts to the transient, dynamically distinct DI. In this study, reanalysis data were combined with observations from the Atmospheric Radiation Measurement Eastern North Atlantic (ENA) site ($39.1^{\circ}N, 28.0^{\circ}W$) to characterize the impact of DIs on MBL characteristics and clouds. Specifically, an objective criterion is applied to the observations made during the winter months of 2016-2018 to identify the DI days from those before and following DIs, and reference periods without DIs. The analyses suggest substantial deepening of the well-mixed boundary layer accompanied by changes in the cloud, precipitation and thermodynamic properties during the DI events. During the DI, the lower troposphere cooled and dried substantially thereby inducing strong surface sensible and latent heat fluxes. All while a strong inversion builds up at the elevated MBL top affecting cloud occurrence. The results show DIs to affect the boundary layer and cloud structure at the ENA site ~21% of the time in winter months, with the response of the cloud fields to the DI-fronts substantially different than that to the non-DI fronts. Hence, the DI events should be considered while studying boundary layer and cloud processes in the region.

1. Introduction

The planetary boundary layer (PBL) is the part of the atmosphere that directly interacts with the underlying surface (Stull, 1988). PBL processes play a role in the modulation of the atmosphere at weather and climate time scales and as such, have an important role in shaping extreme weather and climatic events and in translating their impact onto the surface. In spite of some recent progress, weather and climate prediction models do not realistically represent the processes within the PBL, resulting in biases in the resulting PBL height and the distribution of boundary-layer clouds (Teixeira et al., 2008). The reason being that most of the PBL processes occur at sub-grid scales when compared to typical climate and weather model horizontal grid scales and temporal resolution. Consequently, PBL statistical parameterizations have to be developed (Teixeira et al., 2008). The characteristics of the PBL are determined according to several mechanisms: exchange of heat, momentum, moisture, and chemical constituents between the surface and the free troposphere. Locally-generated buoyancy fluxes and static stability control PBL depth nearly everywhere, though convective mass flux has a large influence at tropical marine locations (Medeiros et al., 2005). Critical to both the local weather conditions and for reliable future climate projections are the accurate modeling of boundary-layer clouds (Sandu & Stevens, 2011; Bony et al., 2015).

Stratocumulus clouds occur during large scale subsidence (Norris, 1998; Norris & Klein, 2000) in subtropical high regions and during cold-air advection (Mechem et al., 2010; Zheng et al., 2020). During the transition (fall and spring) and winter seasons in the midlatitudes, synoptic-scale descent and cold advection mainly occur in the post-cold-frontal regions, i.e., in the cold sector of transient extratropical cyclones and their equatorward trailing cold fronts. The cold sector of the cyclones is characterized by low clouds and strong winds (Field & Wood, 2007; Govekar et al., 2011; Wall et al., 2017). This region is dominated by a slantwise-descending airstream known as the dry intrusion (DI, Carlson, 1980; Browning,

1997). Within DIs, air descends slantwise from the upper troposphere in mid-high latitudes equatorward, reaching the low levels in the cold sector of the surface cyclone downstream, i.e., not locally. *It is important to acknowledge the slantwise nature of the descent of air, in contrast to local subsidence, for understanding how such post-cold frontal environments may impact the PBL.* For example, if originated in the stratosphere, DIs transport high potential vorticity (PV) air to the lower troposphere, thereby reducing the lower-tropospheric static stability below and changing the circulation (Browning & Golding, 1995; Wernli, 1997). However, using a Lagrangian airmass trajectory-based identification of DIs, Raveh-Rubin (2017) showed that almost 99% of DIs are rather tropospheric in their origin. The temperature and moisture contrast of the incoming DI air compared to local conditions in the PBL are potentially key factors for determining their influence. The impact of DIs on the surface weather can be diverse. In the midlatitudes, case studies highlighted the association of DIs with cyclone deepening (Uccellini et al., 1985; Young et al., 1987) and strong wind and precipitation impact near the cold front behind which DIs occur (Carr & Millard, 1985; Browning & Reynolds, 1994). Globally, cold fronts that are associated with DIs are climatologically more intense than cold fronts without DIs association (Catto & Raveh-Rubin, 2019). DIs may enhance precipitation in cyclones through their interaction with moist air ahead of the cold front on the mesoscale, but at the same time can reduce precipitation by its evaporation into the DI airmass (Carr & Millard 1985; Browning & Golding 1995; Raveh-Rubin & Wernli 2016). DIs are further associated with enhanced surface fluxes from the ocean due to the penetration of the incoming dry and cold air (Raveh-Rubin, 2017; Aemisegger & Papritz 2018; Raveh-Rubin & Catto, 2019). Typically, enhanced mixing in the PBL, along with high wind gusts and extreme surface heat and moisture fluxes all co-occur in the presence of DIs when they reach the lower troposphere, inducing potentially unstable regions (Raveh-Rubin, 2017). However, the

influence of DIs on the dynamic and thermodynamic characteristics of the PBL, and its relevance for PBL clouds has not been addressed systematically so far.

Several diagnostic parameters have been proposed that link the coverage of low clouds with the tropospheric stability (Klein & Hartmann, 1993; Wood & Bretherton, 2006; Naud et al., 2020). These indices exploit the fact that a stronger boundary layer inversion is more efficient in capping moisture within the marine boundary layer, permitting greater cloud cover. However, it has been shown that these indices fail to capture the relationship between large-scale environment and cloud cover at sub-daily timescales (de Szoeke et al., 2016; Mechem et al., 2018; Park & Shin, 2019). In the current study we examine the relationship between the large-scale flow and the PBL but depart from the local large-scale stability diagnostics by examining the detailed PBL structure and clouds in response to slantwise descending midlatitude air.

This work utilizes measurements from the Atmospheric Radiation Measurements (ARM) program Eastern North Atlantic (ENA) site ($39.1^{\circ}N, 28.0^{\circ}W$) in the Azores (Wood et al., 2015) sponsored by the U. S. Department of Energy (DOE). This region lies at the southeastern edge of the north Atlantic storm track, where DI occurrence peaks in winter at 6% frequency (Catto & Raveh-Rubin, 2019). Thus, focusing on this region allows a measurement-based investigation of the impact of DIs on the PBL in association with the cold fronts that trail from the transient cyclones, but away from the cyclone center. The ENA site measurement site is unique in the sense that both subtropical and midlatitude synoptic systems govern the area and link to marine boundary layer (MBL) clouds (Mechem et al., 2018; Rèmillard & Tselioudis, 2015). The location of the ENA site is characterized by frequent coverage of MBL low clouds that contribute to the total rainfall significantly (Giangrande et al., 2019). This area is characterized with post cold fronts and non-post cold fronts with both periods generally associated with subsidence and low-level clouds (Naud et al., 2018; Lamraoui et al., 2019).

Yet, during post-cold frontal times, stronger subsidence and wind speed along with weaker inversions and deeper clouds prevail, compared to climatological conditions. Moreover, clouds associated with cold fronts passage contribute 10% more precipitation compared to otherwise subsidence conditions (Lamer et al., 2020).

Since not all cold fronts are followed by deeply-descending DIs, in this study we aim to understand and quantify the transient influence of slantwise-descending DIs on the PBL and its relevance for low clouds. We specifically attempt to address the following questions:

(i) What are the subtropical and midlatitude synoptic systems that host the arrival of DIs into the Eastern North Atlantic in winter?

(ii) Does DI air mix into the PBL? How do the vertical profiles of temperature and humidity evolve during DI events?

(iii) Are surface turbulent heat fluxes modified during DIs, and if so, how?

(iv) How do DI events influence the PBL top height and the inversion properties, namely its height, strength and depth?

(v) How do DI events influence PBL cloud fraction?

2. Methodology

We address the questions by focusing on the months January, February and December of the years 2016-2018 and categorizing the time series in relation to cold fronts and DI events. We combine large-scale atmospheric data and automatic identification of DIs and fronts from reanalysis, with a range of local observations at the ENA site, as detailed hereafter.

2.1 ERA - Interim Reanalysis

We analyze the large-scale atmospheric fields using European Centre for Medium-range Weather Forecasts (ECMWF) ERA-Interim (ERA-I) reanalysis data (Dee et al., 2011).

The spectral data (T255) are horizontally interpolated to a $1^{\circ} \, x \, 1^{\circ}$ grid and 60 vertical hybrid levels, available at 6-h temporal resolution. ERA-I is chosen for this study consistently with the identified cold fronts (see section 2.2). Surface sensible and latent heat fluxes are accumulated in the ECMWF Integrated Forecasting System (IFS) cycle 31R1 that drives ERA-I, using the bulk formulae for the ocean-atmosphere interface (ECMWF, 2007). The height of the PBL is diagnosed in ERA-I using the bulk Richardson method and defined, when scanning from the surface upwards, as the level at which the bulk Richardson number reaches the critical value 0.25.

2.2 Definition of DI events and classification of the time series

Airmass DI trajectories were recently identified globally using a systematic Lagrangian approach. Using LAGRANTO (Sprenger & Wernli 2015), forward trajectories were calculated from a uniform starting grid in ERA-I every 6 h, and a minimum descent threshold of 400 hPa was applied on the 48-h long trajectories to identify DIs among them (Raveh-Rubin, 2017). We use the Lagrangian DI criterion to classify the time series, namely DJF 2016-2018, according to the presence of DIs within a $\pm 1^{\circ}$-radius around ENA measurement site at $39.1^{\circ}N, 28.0^{\circ}W$. First, a 6-h time step is defined as 'DIs' if at least one DI trajectory was detected at the site in the lower troposphere (its pressure level is 700 hPa or larger). The 24-h time window following the last occurrence of DIs is classified as 'post-DIs' (see upper bar in Fig. 1b). Note that if a front or a DI occurred within this 24-h period, the corresponding 6-h time steps are not considered as 'Post-DIs'.

Here we make an important distinction of DIs from any post-cold frontal class. We employ the front identification and DI-matching scheme designed recently in Catto and Raveh-Rubin (2019), where cold fronts were identified in ERA-I using an objective thermal front parameter threshold, based on horizontal gradients of wet bulb potential temperature on the

850-hPa surface. The identified front lines were expanded by 2 grid points in each direction to allow their further classification according to their overlap with a DI behind them. In addition, cold fronts that are geometrically connected to a cyclone were labeled as 'trailing cold fronts' (for further technical details please refer to Catto and Raveh-Rubin 2019). Here, using the same cold front identification technique and DI matching algorithm, we find that all DIs over the ENA site were preceded by detectable fronts (76% of them are trailing cold fronts), such that the time steps before DIs were termed 'Pre-DIs fronts'. As a climatological reference, the remaining timesteps are further divided into Non-DIs with cold front, i.e., when a front that does not match with DIs behind was detected ('Non-DIs-fronts', only 30% of these cases are trailing cold fronts), and the rest as 'Non-DIs' (without any cold fronts, DIs or Post-DIs). The resulting list (Table 1) consists of 63 6-h DI time steps that amount to 31 DI events when aggregating consecutive timesteps with DIs (see Appendix for the list of dates).

Identification	Number of 6-h timesteps	% of time
Non-DIs	649	60.5
Non-DI fronts	196	18.3
Pre-DIs fronts	91	8.5
Dis	63 (31)	5.9
Post-DIs	74	6.9
Total	1073	100

Table 1: The identified classes over the ENA site and their occurrence frequency during the winter study period. The number in parenthesis indicates the number of DIs events.

More generally, to determine where and when DIs reach the lower troposphere on a regional scale, we define 'DI outflows' as regions where any DI trajectories are found at a

given time at a pressure level of 700 hPa or larger. Such DI outflow masks mark the DIs typical location behind the trailing cold front, away from the cyclones center (Raveh-Rubin & Catto, 2019).

2.3 Observational Data Sets

The ARM Climate Research Facility established a permanent observatory in the Eastern North Atlantic (ENA) on the island of Graciosa ($39.1^{\circ}N, 28.0^{\circ}W$) in the Azores, Portugal. Data from several instruments are used in this study to characterize the PBL.

Automatic surface weather station data includes temperature, pressure, humidity and wind, measured at 1-minute intervals. Vertical radiosonde profiles of these variables are routinely available every 12-h (and partially every 6 h) with 10 m vertical interpolation. The Vaisala Laser Ceilometer (CL31) is used with maximum range of 7700 m with 10 m resolution. The ceilometer detects three cloud layers and determines the boundary layer height through the backscatter attenuation (Kotthaus et al., 2016). CL31 ceilometers measure the backscattered light intensity from a pulsed Indium Gallium Arsenide (InGaAs) laser diode transmitter of near infrared wavelength 910 nm as a function of distance. By employing a near infrared wavelength, a pronounced change of the attenuated backscatter profile is mainly attributed to variations in the aerosol content, providing more reliable indicators for clouds and atmospheric layers (Wiegner et al., 2014). In this study, we used the cloud base height and PBL height information from CL31.

Boundary-layer cloud fraction is based on the Ka-band ARM zenith radar (KAZR), a vertical pointing Doppler cloud radar operating 35 GHz (Kollias et al., 2014). The KAZR data were combined with those from the collocated laser ceilometer and the microwave radiometer to derive cloud boundaries based on the Active Remote Sensing of Clouds Locations (ARSCL; Clothiaux et al., 2000) data product. The radar provides radar reflectivity (dBz) in vertical

resolution of 30 m from 160 m up to 18 km with 596 vertical levels and the time interval of measurements is 4 s. Consistent with the sensitivity of KAZR, the hourly values of cloud fraction (CF) were calculated using threshold of -45 dBz (Kollias et al., 2019). In order to avoid contamination from ground clutter, we present the vertical profile from 400 m above surface and upward. Hourly average cloud fraction (CF) was estimated with using a minimum threshold for sensitivity signal pulse (~ -45dBz).

2.4 Observational PBL height estimations and inversion layer detection

Six methods for the estimation of the PBL height are compared. The first five methods detect gradients in the vertical profiles from radiosondes. Here we derive the PBL top from radiosondes at least twice per day when searching from 300 m upwards to 2200 m to avoid temperature inversions near the surface. The PBL height is therefore determined as the 1) Minimum vertical gradient of specific humidity, $\nabla_{min} q$, 2) minimum vertical gradient of relative humidity, $\nabla_{min} RH$, 3) maximum vertical gradient of virtual temperature, $\nabla_{max} T_v$ and 4) maximum vertical gradient of potential temperature, $\nabla_{max} \theta$ following Von Engeln and Teixeira (2013). In addition, a fifth method is based on bulk Richardson number (Seibert et al., 2000; Sorensen et al., 1998) using a threshold of Ri_b=0.25 as in ERA-I. The sixth method uses a retrieval from the CL31 ceilometer where a backscattering attenuation was considered. Up to three distinct heights can be retrieved. We use the second height (named BLH2). The first boundary layer height is typically too close to the surface to be considered, and the third is rarely reported. We further detect the inversion layer properties directly by scanning the radiosonde temperature profile. We then record the inversion layer base height, the inversion depth, and the temperature and specific humidity difference between the inversion top and its base.

3. Results

3.1 An illustrative DI event

A DI event affected the ENA site between 30 December 2017 and 2 January 2018, including the period of Pre-DI, during DI and recovery stage. The DI air mass started its descent near the east coast of North America from 29 December 00 UTC to 30 December 18 UTC, as shown in Fig. 1a specifically for those airmasses that started their descent on 0000 UTC 29 December 2017 (black dots), and reached the lower troposphere around the ENA site 48 hours later. The airmasses descend from the upper troposphere slantwise in the eastward direction over the North Atlantic towards ENA site, where it reached below the 900-950-hPa level (black dots in Fig. 1b), i.e., well inside the PBL. It is insightful to examine the local evolution of the atmospheric column at the ENA site upon the arrival of the DI air and the recovery from it. The Eulerian time-height cross section (Fig. 1b) shows specific humidity, potential temperature and equivalent potential temperature from 28 December 2017 (00 UTC) until 1 January 2018 (18 UTC), which covers all classified categories (upper bar in Fig. 1b). In fact, during this period two cold fronts passed over the site. The first, at 18 UTC 28 December, was not followed by a DI, and the second, on 30 December at 06 UTC, marked the beginning of the DI event. Clearly, the DI event had a substantial signature on the lower troposphere. The specific humidity decreased near the surface from 10-11 $g\ kg^{-1}$ during the cold front to 4-5 $g\ kg^{-1}$ at the peak of the DI event. Moreover, extremely dry air (less than 1 $g\ kg^{-1}$) reached down to the 850 hPa level. The potential temperature (red contours) and equivalent potential temperature (black contours) are almost equal in the dry sector above the PBL. During the DI event, a robust cooling of the entire atmospheric column is observed, while the surface temperature dropped by 15°C. The recovery from the dry and cold surface conditions already started during the DI event itself on 31 December at 18 UTC, presumably due to the strong surface latent and sensible turbulent heat fluxes into the atmosphere (Fig. 2e). Both post-cold

frontal episodes exhibit a pronounced cold θ_e anomaly in the ~700-850 hPa layer. This potential instability is accompanied by a deeper PBL top, consistent with the global mean behavior in Raveh-Rubin (2017). However, the second post-cold frontal episode, governed by the DIs, is accompanied not only by drying, but also by sharp cooling. The mean potential temperature of the DI airmasses decreases slightly from 288.8 K in the northwest Atlantic to 290.2 K at the ENA site (not shown), such that the advection of this airmass and its temperature and humidity content in its origin govern the anomalies observed at the ENA site.

The development of the clouds can be clarified using KAZR radar reflectivity (Fig. 1c). At first, during Non-DIs and Non-DIs-fronts, transient shallow clouds are observed, disconnected from the high clouds above 8 km. During the first cold front (29 December 06-12 UTC) shallow cumulus precipitated rain that reached the ground for a few hours. Compared to the first front, the second front associated with DIs (30 December 12 UTC) had more significant reflectivity with maximum 30 dBz. Rain reached the ground and the clouds top reached up to 10-11 km. From 30 December 18 UTC DIs governed the ENA site for the next 24 h. The near-ground reflectivity was decreased rapidly in the first 6 h of DIs presence. Yet, on the 31 December 00 UTC, when DIs penetrated to low altitude (above 900 hPa, Fig 1b), stratocumulus clouds are sustained without precipitation. The cloud base height in the boundary layer is ~1 km higher compared to the early 'Non-DIs' period on 28 December. Throughout the DIs period, no clouds were observed between 2-8 km. The highest clouds above 8 km occur throughout the five regimes and are likely a result of advection in the upper levels of the troposphere. The reflectivity increases during the Post-DI stage, indicative of precipitation. However, this is related to the eastward propagation of a high-pressure system, accompanied by southwesterly moist flow (not shown). The precipitation at this stage is not related to cold fronts or even post cold front clouds as reported also by Naud et al. (2018).

The evolving synoptic situation is shown by concentrating on the front passage at 12 UTC 30 December (Fig. 2, left column) and on the peak in DIs 12 h later (Fig. 2, right column) according to ERA-I. Initially, during the cold front passage, the ENA site (shown with a red 'x') is influenced by low-level southwesterly moist flow, induced by cyclonic flow to its north, and the edge of the contracted Azores high. The front trails from a cyclone in the North Atlantic with a short wave trough, which later closes near Ireland. A wide upper-tropospheric trough is discernible at front passage (isentropic PV, red contours in Fig. 2a). During the following day, the trough propagates eastwards and narrows due to the ridge that amplifies to its western flank, (Fig. 2b), such that the ENA site is located under anticyclonic environment and strong northwesterly wind behind the trough throughout the troposphere. Under the influence of the DI outflow (magenta contour), the extremely dry lower troposphere (< 1 $g\ kg^{-1}$ at 850 hPa) extends zonally over 20°. The influence of DIs on surface sensible and latent heat fluxes is very pronounced (Fig. 2c, d, negative indicates ocean heat loss to the atmosphere). During DIs, the magnitude of surface heat fluxes increased from about -200 to -400 $W\ m^{-2}$ (latent heat flux) and from 0 to -50 $W\ m^{-2}$ (sensible heat flux) reaching values typically observed farther west over the Gulfstream. Precipitation peaked during the cold front and vanished when DIs dominated the region (Fig 2e, f).

Measurements at the ENA site record the local impact of DI on the surface and PBL, especially under the direct influence of DIs (Fig. 3). During DIs the surface temperature decreased to below 13℃ (Fig. 3b, j). Strong inversion was observed from ~850 (00 UTC) to ~900 (13 UTC) hPa during the day (red lines in Fig. 3b,e,h). Below the inversion, potential temperature is constant, indicative of a well-mixed boundary layer. An inversion was not found during the cold front passage (yellow lines). The mixing ratio (Fig. 3d-f) decreased rapidly under DIs (Fig. 3e), with extremely dry free troposphere, where the mixing ratio is less than 0.5 $g\ kg^{-1}$. Also near the surface, mixing ratio decreased to 4-5 $g\ kg^{-1}$ from 10.5-11 $g\ kg^{-1}$

12 h earlier (Fig. 3d,e,k). Still during the DI event, the mixing ratio increases to 6 $g\ kg^{-1}$ (Fig. 3e; dashed red line and 3k). We attribute this to the peak in latent heat flux from the ocean at this time, supplying new water vapor. It is apparent that the recovery from the DIs (1 January) occurred up to the inversion but without changes in the free atmosphere. Changes to the higher levels occurred only after the weakening of the inversion during Post-DIs (Fig. 3f; cyan lines) until reaching back to the average conditions (Fig. 3f; gray line). The relative humidity (Fig. 3g-i) evolution provides clues for the maintenance of PBL clouds despite the drop in mixing ratio. Lower-tropospheric RH drops from more than 80% to 40-60% (Fig. 3g, I; gray lines). DIs decrease the relative humidity to 40-60% near the surface and 60-80% below the inversion (Fig. 3h,i). The relative humidity below the inversion remains high enough due to relatively cold air and the isolated MBL due to the strong inversion allowing MBL clouds also during DIs (Fig. 1c). Precipitation, however, occurs during the cold front together with peaking surface winds and a drop in surface pressure (Fig. 3m-o).

3.2 Mean large-scale environment and surface turbulent heat fluxes

We infer the mean large-scale configuration of the synoptic systems by averaging the meteorological maps for each DI-relative class during the study period. Large-scale anticyclones govern the ENA site throughout the year (Wood et al., 2015). However, any changes of the location and the strength of the system leads to significant modification of the governing airmasses at ENA site. Figure 4 shows the average SLP, isentropic PV, 850-hPa specific humidity along with the mean location of cold fronts (blue contour) and DI outflows (magenta contours). Without DIs, the ENA site lies in the northwestern quarter of the surface anticyclone, away from the ridge-shaped dynamical tropopause (Fig. 4a). The mean position of DIs and cold fronts to the west reflect their climatological distribution in DJF (Catto & Raveh-Rubin, 2019), consistent also with Naud et al. (2018, their Fig. 1c). When cold fronts

cross the ENA site, specific humidity reaches the highest values 5-6 $g\ kg^{-1}$ which is spatially connected to the tropical moisture reservoir in the western Atlantic in both Non-DIs-fronts and Pre-DIs fronts categories (Fig. 4b-c). However, major differences emerge between the two front cases. On average, when DIs follow the front, the cyclone in the north Atlantic is deeper and larger, and the anticyclone is less pronounced, compared to cold fronts with no DIs. This difference is induced by a more pronounced trough in the upper troposphere and overall result in stronger SLP gradients and longer fronts, as also noted recently by Raveh-Rubin and Catto (2019). Part of the difference can be attributed to the larger fraction of trailing fronts in the Pre-DI fronts category, compared to Non-DI fronts (see Section 2.2). The driest mean (2 $g\ kg^{-1}$) around ENA site was observed during DI events (Fig. 4d) with slight increase in the period of Post-DIs (Fig. 4e). During DIs, and further under Post-DIs, the aforementioned trough propagates eastward, along with the low-pressure systems and the associated front. Under these conditions, the ENA site is positioned under the on-setting ridge, and on the northeastern side of the surface anticyclone, which itself dislocated westwards and intensified to over 1028 hPa in its center. The average SLP map of the 'DIs' period is similar to the map in Naud et al. (2018, their Fig. 1a), where the ENA site is influenced by post-cold-frontal northwesterly winds.

The ENA site is located away from sharp SST gradients, such that the mixing of dry and cold DIs air into the MBL can enhance the mean latent and sensible heat fluxes from the ocean over the site (Fig. 5). Climatologically, with no DIs, the strongest surface fluxes occur over the warm ocean currents in the western Atlantic (Fig. 5a). The surface fluxes over the ENA site remain low in both cold fronts' cases (Fig. 5b, c), but in the Pre-DI case the fluxes behind the fronts are more intense in the location of the DIs outflow (Fig. 5b, c). DI events lead to strongest effect in terms of surface fluxes, when the average latent and sensible heat fluxes reach -200 $W\ m^{-2}$ and -40 $W\ m^{-2}$, respectively (Fig. 5d). The intense surface fluxes weaken

during the Post-DIs over the islands (Fig. 5e), however, the intense fluxes during DIs are consistent with the recovery of the humidity deficit induced by the DIs in its post-stage (Fig. 4d, e).

To understand the variability of the surface fluxes under the different dynamical classes, figure 6 shows the frequency after binning for the intensity of latent (Fig. 6a) and sensible (Fig. 6b) heat fluxes (only negative values are presented, omitting the minus sign). Both non-DI classes peak in low heat fluxes and their frequency of stronger fluxes decreases dramatically. The major shift in the distribution towards intense fluxes occurs during DIs, with hardly any weak fluxes and a clear dominance of the strongest flux magnitude (stronger than -160 and -40 $W\ m^{-2}$ for latent and sensible heat fluxes, respectively) compared to other classes. The Post-DI stage still exhibits strong fluxes, although the distribution is shifted to weaker values compared to the DIs period.

Enhanced surface heat fluxes provide buoyancy for upward vertical motion within the PBL, promoting its deepening. The mean PBL height variability under the different dynamical classes can be therefore examined (Fig. 6c) based on ERA-I. The PBL height distributions of the DIs and Post-DIs are oppositely skewed compared to the distributions during Non-DIs and during the front categories. DIs capture the maximum frequency at 1.4-1.6 km. The most frequent PBL height under Non-DIs and Pre-DIs conditions is 0.6-0.8 km, with less than 5% frequency for PBL heights beyond 1.4 km. In contrast, the most frequent PBL height under DIs is 1.4-1.6 km, a with second peak at 0.8-1.0 km. The highest PBL height occurs almost exclusively under DI conditions. The PBL height during the Post-DIs stage is distributed similarly but with decreased heights compared to DIs, with peak frequency between 1.2-1.4 km. In the next section we focus in more detail on the local conditions under the different classes. Collectively the figure suggests the boundary layer to be much deeper, forced by high surface fluxes during DIs as compared to the other environmental scenarios. Somewhat

surprisingly, vertical velocity at 850 and 700 hPa (not shown), is not strongly differentiated among the categories. However, at the 500-hPa level (i.e., above the PBL), the highest occurrence of subsidence was found under DIs (Fig. 6d), consistent with the high-pressure systems strengthening there at those times, compared to the frontal passage (Fig. 4e). Yet, for all dynamical categories omega is distributed with both negative (ascent) and positive (subsidence) values.

3.3 Impact of DIs on surface conditions based on ARM-ENA data

The impact of DIs on local PBL characteristics at the ENA site is first explored on the (near) surface conditions. Climatologically, the prevailing 50-m above-ground level (AGL) wind directions are southerly and south-westerly (Fig. 7). The mean surface wind direction can be generally explained by the synoptic situation and the shifting mean location of the low to the north and that of the high-pressure system to the south of the ENA site (Fig. 4). Uniquely, during DI events the direction of wind shifts after the cold front passage to north-westerly. The northerly (and even northwesterly) wind component remains during Post-DIs, however the climatological south-westerly component already builds up during this stage.

The distinct advection into the ENA site during DIs creates a signature on surface measurements of other meteorological parameters. Hourly surface measurements were attributed to each dynamical class by considering the ±3 h period around each 6-h time step. The resulting distributions of surface pressure, temperature, relative humidity, specific humidity and wind speed are given for each dynamical class in Fig. 8. The median surface pressure is lowest during the two front classes, namely 1013.3 hPa during Pre-DIs fronts and 1016.6 hPa during Non-DIs-fronts. The highest median pressure occurs during DIs (1026.28 hPa), but the highest value extreme (95^{th} percentile) is observed at the Post DIs stage. The results are consistent with the reanalyzed SLP from Fig. 4.

The illustrative case (Section 3.1) demonstrated a cold surface anomaly during DIs. Here, surface measurement confirm that the coldest surface temperatures are observed during DIs and Post-DIs, and the median temperature is lowest (~14℃) at the ENA site during DIs (Fig. 8b). Specific humidity is clearly the lowest during DIs and maintains the narrowest distribution compared to all other categories. The dryness dominates the relative humidity signal during DIs, such that RH is lowest as well, despite the relatively low temperature then (Fig. 8c, d). The strongest surface wind speed is observed during Pre-DIs fronts and DIs, exceeding median values of 7 $m\ s^{-1}$. The reduction of the wind speed is shown later during the 'Post-DIs' with 5.7 $m\ s^{-1}$, and the lowest wind speeds are measured with no DIs. Finally, cloud base height (CBH) is determined based on the ceilometer. The maximum median of the CBH occurs during DIs (~1330 m AGL). At the Post-DIs stage median CBH reduces by 200 m, while lower values and wider variability occurs with Non-DIs. The cold fronts categories do not represent well the CBH due to precipitation. This aspect will be elaborated in Section 3.6.

3.4 Impact of DIs on vertical profiles in the PBL based on ARM-ENA radiosondes

In order to quantify and understand how the vertical PBL profiles are shaped under DIs, we average all available radiosonde data separately for each class. The vertical profiles of temperatures, humidity and wind speed up to 5 km are shown in Fig. 9. The vertical profiles of temperature mark the presence of a marine inversion layer in all cases except for fronts (Fig. 9a). However, weak inversion layers were found in fronts with various altitudes when scanning the individual profiles, but were smoothed out in the averaging process. The smallest inversion that can be detected is 10 m. The mean altitude of the marine inversion is lowest under 'Non-DIs' at ~1 km above the surface presumably again partly due to smoothing by the averaging process. In contrast, during DIs, the inversion is clearly located higher above 1.5 km and the

gradient of temperature above this level is very sharp. The altitude of the inversion decreases to around 1.2-1.3 km and its mean signature weakens in the Post-DIs stage, but still stronger gradient and higher altitude than at Non-DIs. Importantly, the coldest temperature from the surface up to 3 km occur under DIs. The clear local cold anomaly at the ENA site means that despite the adiabatic warming the DI air parcels experience during their descent, the advected DI air is still colder than the in-situ air, which can also be observed by the profile of potential temperature (Fig. 9b). Potential temperature is almost constant in the lowest 1.5 km of the troposphere during DIs, indicating a deeper well-mixed layer, compared to the other classes. The maximum gradient of potential temperature is located around 1.5 km, consistent with the inversion height (Von Engeln & Teixeira, 2013). The vertical profile of equivalent potential temperature (Fig. 9c) shows large differences among the classes, combining their temperature and humidity differences together. The lowest equivalent potential temperature is found during DIs. The mean vertical gradient of θ_e suggests that potential instability prevails below the inversion layer, above which θ_e increases with height, most strongly under DIs. The profile of mixing ratio highlights the utterly dry free troposphere during DIs, and the dilution of PBL mixing ratio by the mixing of the DI air into it (Fig. 9d). Overall, during DIs the mixing ratio is the lowest throughout the atmospheric column, and decreases from $6\ g\ kg^{-1}$ at the surface up to $1 g\ kg^{-1}$ above the top of the inversion around 2 km. The recovery from the extreme dryness occurs mainly near the surface and above the inversion in the Post-DIs stage, but the mixing ratio is still lower compared to Non-DIs or the moist frontal categories. Interestingly, the combined effects of temperature and mixing ratio result in a nearly-constant relative humidity PBL profile in Non-DIs and fronts classes, and an increasing RH with height during DIs, when maximum RH is recorded at 1.5-2 km (Fig. 9e). In contrast, the reduction of RH with height above the inversion layer occurs for all classes, but it is dramatic during DI, with a

sharp mean drop from >80% to ~15% over ~100 m, compared to the mean decrease from 80% to 20% over 2-km height for the other classes.

The vertical profiles of horizontal wind speed show maximum winds during the passage of cold fronts (Fig. 9f), when the strongest pressure gradient forces prevail (Fig. 4). After fronts, it is DIs which host the strongest winds up to the top of the PBL around 2 km. However, above the PBL, the strongest winds occur during DIs, followed by fronts and Post-DIs, while the weakest wind speeds in the free troposphere occur during Non-DIs. It is important to remember that it may be misleading to infer mechanistic understanding from mean properties, so in the next section we diagnose the PBL height and the inversion based on the individual profiles.

3.5 PBL height and inversion properties

It is instructive to estimate the PBL height in the different dynamical regimes, based on the individual time steps, rather than by means of smoothed averaged profiles. There are several methods for the estimation of the PBL height from radiosonde and ceilometer data. Employing six methods described in Section 2.4, figure 10 shows the resulting PBL height distributions according to each method and dynamical class. The Ri_b-based method suggests the lowest PBL height compared to the other methods, the ceilometer-based method BLH2 provides the second lowest, compared to the four gradient-based methods. Despite the differences among the methods, clear trends can be identified when contrasting the dynamical classes, consistent across methods. During DIs, all methods agree that PBL height is higher by 300 m on average compared to other times. The gradient methods agree better among themselves when the inversion layer is strong, which occurs most often during DIs and Post-DIs, but less during frontal passages when there is only weak inversion due to instabilities.

We further characterize the inversion layer itself from the radiosondes data (Section 2.4). In most DI and Post-DI cases, the inversion layer is located between 900 hPa and 800

hPa. Referring to the large-scale conditions on the lower-tropospheric stability, here we specifically diagnose the inversion strength (IS) as the temperature difference (ΔT) or mixing ratio difference (Δq) between the top and bottom (base) of the inversion layer. The inversion depth was determined for the inversion thickness with at least 50 m. The distribution of the inversion base (IB) is binned for the range 0.7 - 2.2 km with intervals of 0.3 km (Fig. 11a). Consistent with the PBL height estimations, during DIs the IB distribution is strongly skewed towards the highest values with over 40% of the time in the largest bin (1.9-2.2 km). Together with the adjacent bin (1.6-1.9 km) almost 80% of DI cases have an inversion base higher than 1.6 km. Already at the Post-DIs stage, the distribution of IB is more even, peaking at 1.3-1.6 km, similar to the Non-DIs group. In fact, a skewed distribution of IB towards the high values is already discernible during Pre-DIs fronts, more than at Non-DIs-fronts, although small. However, significant differences between the two front groups were found according to the IS calculation. Both the Δq and ΔT (from 1.5 to more than 5.5 difference bins with 1 interval) distributions indicate clearly weaker IS during Pre-DIs fronts compared to Non-DI-fronts (Fig. 11b), a difference that could not be identified by observing the aggregated profiles (Fig. 9). In over 70% of the time at the Pre-DIs fronts stage, the IS lies in its weakest bin, compared to ~30% for both Non-DIs fronts and generally for Non-DIs categories. This situation quickly changes upon the DI and Post-DIs regimes, when the IS is more often stronger, partially dominating the strongest IS bins (Fig. 11b,d). Inversion depth was tested with interval of 50 m from 50 to 250 m. The long-tailed distributions of the inversion depth during DIs and Post-DIs indicate that they occur frequently with a thick inversion layer (up to 200 m, Fig. 11c), in addition to being generally higher and stronger during these cases, compared to other times, when the most common depth is less than 100 m.

3.6 Radar Reflectivity and cloud fraction

Considering the dramatic influence of the arrival of DIs on PBL characteristics, it is expected that the low-level cloud fraction responds in a coherent manner as well. The stratocumulus cloud regime dominates over the ENA site (Rèmillard et al., 2012; Wood et al., 2015; Yang et al., 2018). Therefore, low reflectivity is usually observed in this area. Clouds develop during the cold fronts crossing of the island, leading to increase of the reflectivity. We assemble data from KAZR-ARSCL for each category by plotting the contour frequency altitude diagram (CFAD). The results show marked differences among the groups (Fig. 12). The climatology (Fig. 12a) shows that high frequency is reported between 0.6 to 1 km with low reflectivity within a range indicative of condensation and cloud formation inside the MBL (-40 to -20 dBz). In contrast, the peak under DIs is around -20 dBz between 1.5 to 2 km (Fig. 12d). During DIs, reflectivity values below 0 dBz are absent altogether between 2-5 km, suggesting the evaporation of droplets and drizzle under the dry conditions. The peak reduces to 1-1.5 km after the DIs and shifts to slightly lower than -20 dBz (Fig. 12e). The comparison between the cold fronts with DIs (Fig. 12c) and without DIs (Fig. 12b) is highlighted. The slight difference in the reflectivity indicates that in all groups (except fronts), clouds remain stratiform without significant convection. High reflectivity during the 'Pre-DIs fronts' suggests rain with clouds developing up to 4 km (peaking between 2 to 3 km). These findings are consistent with those from Giangrande et al. (2019) of the low clouds being most frequent with south-north westerly winds and higher cloudiness during northerly wind component.

The cloud fraction for each group was averaged for each height based on hourly CF calculations from KAZR-ARSCL (Fig. 12f). The profiles indicate that the CF in all categories resemble the classical stratocumulus-topped boundary layer structure with cloudiness increasing with height from the surface up to the top of the PBL. The sharp decrease of CF in DIs and Post-DIs suggests low entrainment from the free troposphere to the clouds at the top

of the PBL. In contrast, weak slopes from the maximum CF to higher levels were found during the fronts. A clear signal of enhanced CF during the integrated DI event (i.e., Pre-DI-fronts, DIs and Post-DIs) is evident when comparing to Non-DIs CF. Above 0.7 km altitude, CF maxima reach 0.4 on average during the integrated DI episodes, while it is less than 0.3 during both 'Non-DIs' categories. At peak time, during DIs, the mean CF maximum is located at the highest altitude, ~1.5 km, compared to all other times.

3.7 An integrated view on the time evolution of DI events

Considering all aspects concerning the impact of DI events on the PBL at the ENA site, here we summarize the main findings by considering the evolution of the PBL from Non-DI background conditions, to a Pre-DI-front passage, a DI event and a Post-DI recovery phase. To this end we composite the atmospheric profile at the ENA site through 48 h before and after the DIs first arrival at the site. By considering all 31 DI events, Fig. 13 shows the mean time evolution with respect to DI first arrival (relative time 0, vertical red line). On average, 18-24 h before the arrival of DIs, the warmest surface air temperatures occur, followed by a temporal peak in specific humidity throughout the lower and mid-troposphere at -12 h. From this instance, based on ERA-I, specific humidity and temperature drop sharply throughout the atmospheric column up to the 300 hPa level (shown up to 500 hPa), until reaching their minima at +6 h on average. Near the surface, specific humidity drops by more than 48% during 30h (Fig. 13a). Dry air (less than $1\ g\ kg^{-1}$) penetrates down to pressure levels greater than 700 hPa. The black points mark the highest pressure that DIs reached (average for all events for each relative time step). Re-moistening of the near surface becomes evident after about +20 h following the arrival of the DIs and gradually propagates upward. Mean PBL height (Fig. 13b), peaks at 0 h and then starts decreasing. Sensible and latent heat fluxes were examined locally from ERA-I (Fig. 13c,d), as no such ocean observations are available from the ENA site. The

recovery phase (i.e. a decrease in absolute value of the fluxes) starts almost immediately at +6 h, but the fluxes remain relatively intense up to +48 h, as they are still stronger then compared to at -48 h. Surface measurements further highlight the drop in temperature, specific and relative humidity between -12 and +6 h, which is accompanied by a peak in the 10-m wind speed and increasing surface pressure (Fig. 13e). On average specific humidity and relative humidity drop by more than 35% and 20% respectively. The temperature decreases by more than 14% and wind speed increases by more than 17%. During 0-30 h, cloud base height is maximal, around 1300 m, consistent with the relatively dry and deep PBL, compared to ~1000 m otherwise. During that period, the cloud base height increases around ~10%.

4. Discussion and conclusions

The ENA site is located on the southeastern edge of the North Atlantic storm tracks. Hence the transient influence of troughs in the midlatitude Rossby wave guide, and the accompanying surface cyclones and trailing cold fronts, can be studied through the occurrence of dry intrusions, in which airmasses descend slantwise into the PBL at the ENA site. Overall, during DJF of 2016-2018, DI events influence the ENA site for more than 21% of the time, including its Pre- and Post-DI stages, reflecting the significant fraction of time that the ENA site experiences the DI-related impact. We make an important distinction between common subsidence conditions and the slantwise descent of air within DIs. *Despite warming during the descent, DIs are associated with cold-air advection and reach the ENA site colder than in situ air, in contrast to warm anomalies caused by locally-subsiding air*.

The impact of DIs on the PBL is summarized in the schematic in Fig. 14, and in the following points with respect to the questions (i)-(v) posed in the introduction.

(i) Generally, without the influence of DIs, a high-pressure system to the south east governs the conditions at the ENA site, such that the site is under quiescent

southwesterly flow. The arrival of the cold front is accompanied by an upper tropospheric trough, deepening in the western North Atlantic, together with the weakening and eastward propagation of the surface anticyclone. In the cases followed by DIs, a significant deepening of the cyclone to the north (60°N 30°W) occurs with increased surface pressure gradient (i.e., compensating the weakening of the surface high pressure to the south). During DIs, the trough has propagated eastwards, such that the surface winds have uniquely a northerly component. At this stage, the anticyclone strengthened and the pressure gradient remained strong. The Post-DI stage is characterized by an anticyclone to the south and west of the ENA site (compared to the general south and eastern location), and a ridge in the upper tropospheric jet dominating the N. Atlantic.

(ii) The DI air mixes into the PBL, thereby cooling and drying the entire atmospheric column, and particularly within the PBL. Under DIs, the lapse rate follows closest to the dry adiabatic values, and thus the potential temperature profile is nearly constant up to ~1.5 km. Above 2 km, the median mixing ratio is uniformly lower than 1 g kg^{-1} under DIs. In the PBL the DI air dilutes and replaces the anomalously moist PBL at frontal passage, such that the mixing ratio decreases slowly with height close to the surface, and more rapidly closer to 2-km altitude. Overall, the mixing ratio is lowest during DIs compared to all other times in winter.

(iii) DIs are associated with enhanced turbulent surface heat fluxes into the atmosphere, both sensible and latent. The average sensible and latent heat fluxes are -40 $W\ m^{-2}$ and -200 $W\ m^{-2}$ during the DI events, respectively, compared to -10 $W\ m^{-2}$ and -80 $W\ m^{-2}$ mean climatological magnitudes respectively. It is presumably the strong humidity deficit that enhances ocean evaporation, and the cold air contrast with the warmer sea-surface temperature that enhances the sensible heat fluxes. In

addition, surface wind speed is somewhat enhanced during DIs, and the relative contribution of the winds to the overall fluxes is yet to be quantified in future work.

(iv) The PBL height was higher during the DIs compared to all other times. Although high variability occurs, it should be noted that the relatively robust inversion signature during DIs allows the reliable determination of the PBL top, compared to times of frontal passage. On average, during DIs the inversion base is higher (1.9 km on average, compared to 1.3 km when no DIs occur), and it is deeper (30% of the time above 150 m, compared to <100 m being the most frequent depth in other times). In addition, during DIs the inversion strength is greater both in terms of temperature and humidity difference across the inversion.

(v) The cloud fraction is high during DIs peaking with almost 40% at 1.5-km altitude, compared to less than 15% at this height when no DIs are present. However, below 1 km, CF is lowest during DIs, indicating the relatively elevated cloud layer. Overall, taking into account the whole DI event, i.e., pre-DI frontal passage, the DI and post-DI stage, CF increased from 0.28 to 0.38 on average during the events. The general increase of CF is consistent with the positive correlation between CF and the inversion strength. In the absence of advection, elevated PBL height generally corresponds to lower CF (Bretherton and Wyant 1997, Zheng et al. 2018) however that is not the case during DIs in which advection is dominant. Here the free tropospheric DI air is relatively cold, such that its mixing into the BPL explains both the elevated PBL top height and the strong inversion, corresponding to a different decoupling scenario compared to pure entrainment of dry air through the (weak) inversion.

The properties of boundary layer and those of the clouds within are thought to be modulated by largescale properties within the column and those occurring at mesoscales, while

recent literature shows that these properties are also modulated by synoptic scale features (e.g. McCoy et al., 2017; Naud et al., 2018). The results presented in this study highlight that not all synoptic scale features (cold fronts) have similar impact on the boundary layer structure and the clouds, as highlighted by the differences between DI fronts and non-DI fronts. Hence, careful considerations must be placed regarding the origin, type and strength of the cold fronts while studying their impacts on the clouds in the region.

The focus on a single site in the eastern North Atlantic suggests coherent responses of the PBL to large-scale dry intrusions from the midlatitude free troposphere. However, other geographical locations, or other locations relative to typical cyclone life cycle and track may show a different response. Raveh-Rubin (2017) found a robust deepening of the PBL in many other regions, based on ERA Interim, suggesting that some findings can be representative for other regions as well. However, the unique aspects controlling cloud response to this particular flow feature should be considered carefully in future studies.

The increase in the surface fluxes during and after the DI event are due to the drying and cooling from the DI, thereby bringing the boundary layer thermodynamic structure to the pre-DI conditions. It is unclear whether Earth System Models (ESM) or Numerical Weather Prediction (NWP) models accurately capture the evolution of DI and its interaction with the PBL. Further, heavy precipitation and precipitation-induced density currents are known to exist during the post-frontal (and DI) conditions in the region (Ghate et al. 2020). It is unclear how these cloud systems persist for longer periods despite having considerable precipitation rates and high diabatic cooling. Studies utilizing Large Eddy Simulations (LES) models together with detailed observations might shed more insights on the interactions of DIs with surface fluxes clouds, and PBL structure.

Data Availability Statement

The ERA-Interim data was obtained from the ECMWF website. https://www.ecmwf.int/en/forecasts/datasets/reanalysis-datasets/era-interim. All ARM data sets used (sounding profiles, meteorological station, ceilometer and cloud radar vertical profiles) can be downloaded at https://adc.arm.gov/discovery/.

Acknowledgements Data were obtained from the Atmospheric Radiation Measurement (ARM) user facility, a U.S. Department of Energy (DOE) office of science user facility managed by the biological and environmental research program. The Israel Meteorological Service and ECMWF are acknowledged for providing access to ERA-Interim data. This research was supported by the Israel Science Foundation (grant No. 1347/18) and the Karen Siem Fellowship for Women in Science, and partially supported by the Israeli Council for Higher Education (CHE) via the Weizmann Data Science Research Center, and by a research grant from Madame Olga Klein – Astrachan. VG was supported by the National Aeronautics and Space Administration (NASA) grant 18-ACMAP18-0110 awarded to the Argonne National Laboratory, and the U.S. Department of Energy's (DOE) Atmospheric System Research (ASR), an Office of Science, Office of Biological and Environmental Research (BER) program, under Contract DE-AC02-06CH11357 awarded to Argonne National Laboratory. We gratefully acknowledge the computing resources provided on Bebop, a high-performance computing cluster operated by the Laboratory Computing Resource Center (LCRC) at the Argonne National Laboratory. Finally, we thank three anonymous reviewers whose suggestions improved the clarity of the manuscript.

Appendix. List of the DI events

Number of event	Date (initial time, UTC)	Event duration (hours)
1	04-Jan-2016, 12:00	6
2	07-Jan-2016, 12:00	6
3	10-Jan-2016, 06:00	18
4	11-Jan-2016, 06:00	12
5	27-Jan-2016, 12:00	12
6	14-Feb-2016, 00:00	18
7	16-Feb-2016, 18:00	24
8	03-Dec-2016, 12:00	6
9	13-Dec-2016, 12:00	18
10	15-Dec-2016, 00:00	36
11	18-Dec-2016, 12:00	30
12	01-Feb-2017, 12:00	18
13	06-Feb-2017, 06:00	12
14	07-Feb-2017, 06:00	6
15	09-Feb-2017, 00:00	24
16	11-Feb-2017, 12:00	6
17	11-Dec-2017, 06:00	12
18	25-Dec-2017, 06:00	18
19	30-Dec-2017, 18:00	30
20	04-Jan-2018, 12:00	6
21	05-Jan-2018, 12:00	12
22	09-Jan-2018, 00:00	12

23	24-Jan-2018, 12:00	24
24	06-Feb-2018, 06:00	18
25	23-Feb-2018, 18:00	6
26	25-Feb-2018, 12:00	6
27	05-Dec-2018, 00:00	12
28	10-Dec-2018, 18:00	24
29	12-Dec-2018, 06:00	30
30	15-Dec-2018, 00:00	12
31	17-Dec-2018, 18:00	36

Table. A1. The dates of the 31 DI events for December-February between 2016 - 2018.

Figure captions

1	**Fig. 1.** A selected DI event from 28 DEC 2017 00 UTC to 01 JAN 2018 18 UTC. (a) DI trajectories starting their 48-h long descent at 12 UTC 29 DEC 2017, colored according to their pressure level (hPa). The black dots mark the location of the trajectories at initial time. The red 'x' marks the location of the ENA site. (b) Time-height cross section of specific humidity ($g\ kg^{-1}$; shaded), potential temperature (K; red contours), equivalent potential temperature (K; black contours) and boundary layer height (blue line) at the ENA site (39.1^oN,28.0^o W). The black dots mark the pressure level of DI trajectories when present within a 1-degree radius around the ENA site. Data are taken from ERA-I. (c) Retrieval of KAZR radar reflectivity (dBz).
2	**Fig. 2.** Atmospheric parameters during two stages of the DI event, 12 UTC 30 December 2017 (pre-DI stage, left column) and 00 UTC 31 December 2017 (DI stage, right column). (a,b) Specific humidity ($g\ kg^{-1}$) at 850 hPa, SLP (black contours, at 5-hPa intervals), wind arrows at 850 hPa (red arrows for wind speeds exceeding 10 m s^{-1}). PV on the 315 K isentropic surface is overlaid (2 and 3 PVU in red solid and dashed contours, respectively). (c,d) Surface latent heat flux ($W\ m^{-2}$, shaded), surface sensible heat flux (black contour, at 50 $W\ m^{-2}$ intervals). Negative indicates ocean heat loss to the atmosphere. (e,f) Total accumulated precipitation over the preceding 6 h (mm) from ERA-I. In all panels, the red 'x' marks the location of the ENA site, DIs outflow is encircled by the magenta contour, and the expanded cold front region is marked by the blue (a,b), green (c,d) and black (e,f) contour.

3	**Fig. 3.** Radiosondes vertical profiles of (a-c) potential temperature (℃), (d-f) water vapor mixing ratio ($g\ kg^{-1}$), and (g-i) relative humidity (%) for difference time. Hourly time evolution of **s**urface measurements: (j) temperature (℃), (k) water vapor mixing ratio ($g\ kg^{-1}$), (l) relative humidity (%), (m) pressure (hPa), (n) wind speed ($m\ s^{-1}$) and (o) rain rate ($mm\ hr^{-1}$). The red stars in (j)-(o) mark the time of DIs.
4	**Fig. 4.** Composite specific humidity ($g\ kg^{-1}$) at 850 hPa overlaid with the 2 and 3-PVU on the 315K isentropic surface (solid and dashed red contours, respectively) and SLP (black contours, at 2 hPa intervals) for all categories: (a) Non-DIs, (b) Non-DIs-fronts, (c) Pre-DIs fronts, (d) DIs, and (e) Post-DIs. In all panels, the red 'x' marks the location of the ENA site, DIs outflow is encircled by the magenta contour, and the expanded cold front region is marked by the blue contour. Data are from ERA-Interim for DJF 2016-2018.
5	**Fig. 5.** Composite surface latent heat flux ($W\ m^{-2}$) overlaid with sensible heat fluxes (black contours, at 20 $W\ m^{-2}$ intervals) for all categories: (a) 'Non-DIs', (b) 'Non-DIs'-fronts, (c) Pre-DIs fronts, (d) DIs, and (e) Post-DIs. In all panels, the red 'x' marks the location of the ENA site, DIs outflow is encircled by the magenta contour, and the expanded cold front region is marked by the green contour. Data are from ERA-Interim for DJF 2016-2018.
6	**Fig. 6.** Frequency distribution of (a) surface latent heat flux ($W\ m^{-2}$), (b) surface sensible heat flux ($W\ m^{-2}$), (c) boundary layer height (km) and (d) 500-hPa Omega ($Pa\ s^{-1}$) from ERA-Interim, averaged within the 9 one-degree grid points around the

	ENA site i.e. $38^o - 40^o$N and $29^o - 27^o$W. The frequency is normalized for each class.
7	**Fig. 7.** Wind directions histograms from radiosondes at the lowest altitude of measurements (50 m A. G. L.) for the categories (a) Non-DIs, (b) Non-DIs fronts, (c) Pre-DIs fronts, (d) DIs, and (e) Post-DIs. Northerly wind is indicated by 0 degrees. Please note that the length of the bars in the radial direction indicates the frequency of occurrence for each direction, and not the wind magnitude.
8	**Fig. 8.** Distributions of surface measurements of atmospheric parameters for the different categories: (a) Pressure, (b) temperature, (c) relative humidity, (d), water vapor mixing ratio, (e), horizontal wind speed, and (f) Cloud base height. The thick horizontal line marks the median value of distributions. The boxes correspond to 25^{th} and 75^{th} percentiles of the distributions, the whiskers to the 5th and 95th percentiles and the red crosses mark the outliers.
9	**Fig. 9.** Radiosondes vertical profiles of (a) air temperature, (b) potential temperature, (c) equivalent potential temperature, (d) water vapor mixing ratio, (e) relative humidity, and (f) horizontal wind speed. The solid lines are the median value at each height and category, and the shaded area marks the range between the 25^{th} and 75^{th}percentiles of the Non-DIs and DIs distributions.
10	**Fig. 10.** PBL height (km) distributions according to six methodologies for each dynamical category. Five definitions are based on radiosondes data: Ri uses the bulk Richardson threshold of 0.25, four gradient definitions follow Von Engeln and

	Teixeira (2013). BLH2 is additionally derived from independent ceilometer data (see Section 2.4 for exact definitions). The boxes correspond to 25^{th} and 75^{th} percentiles of the distributions, the whiskers to the 5th and 95th percentiles and the red crosses mark the outliers.
11	**Fig. 11.** Frequency distribution of (a) inversion base height (km), (b) mixing ratio difference between the bottom and top of the inversion layer (g kg^{-1}), (c) inversion depth (m), and (d) temperature difference between the top and bottom of the inversion layer (k) based on radiosondes, for all categories.
12	**Fig. 12.** The CFAD of radar reflectivity from KAZR. (a) Non-DIs, (b) Non-DIs fronts, (c) Pre-DIs fronts, (d) DIs, (e) Post-DIs. (f) Vertical profile of mean hourly cloud fraction estimated from KAZR, averaged for each dynamical class.
13	**Fig. 13.** Composite temporal evolution of 31 DI events. Relative time 0 h marks the initial occurrence of DIs within a 1-degree radius of the ENA site (shown with a vertical red line). Shown are (a) mean time-height cross section of specific humidity (g kg^{-1}), potential temperature (K, red contours) and equivalent potential temperature (K, black contours) from ERA Interim. Also shown is the event distribution of the highest DI pressure recorded at each relative time step (black points). (b) Time series of PBL height (km) based on Bulk Richardson number of 0.25 in ERA-Interim (solid black) and ENA-site radiosondes (blue points at 12-h intervals). (c) Surface latent heat fluxes and (d) surface sensible heat fluxes ($W\ m^{-2}$), from ERA-Interim data. The vertical lines in (b-d) mark the standard deviation. Time evolution of average meteorological surface measurements: (e) pressure (hPa), temperature (°C) and wind

	speed ($m\ s^{-1}$), (f) mixing ratio ($g\ kg^{-1}$), relative humidity (%) and cloud base height (m).
14	**Fig. 14.** Schematic summary of MBL characteristics at the ENA site for each category.

Figures

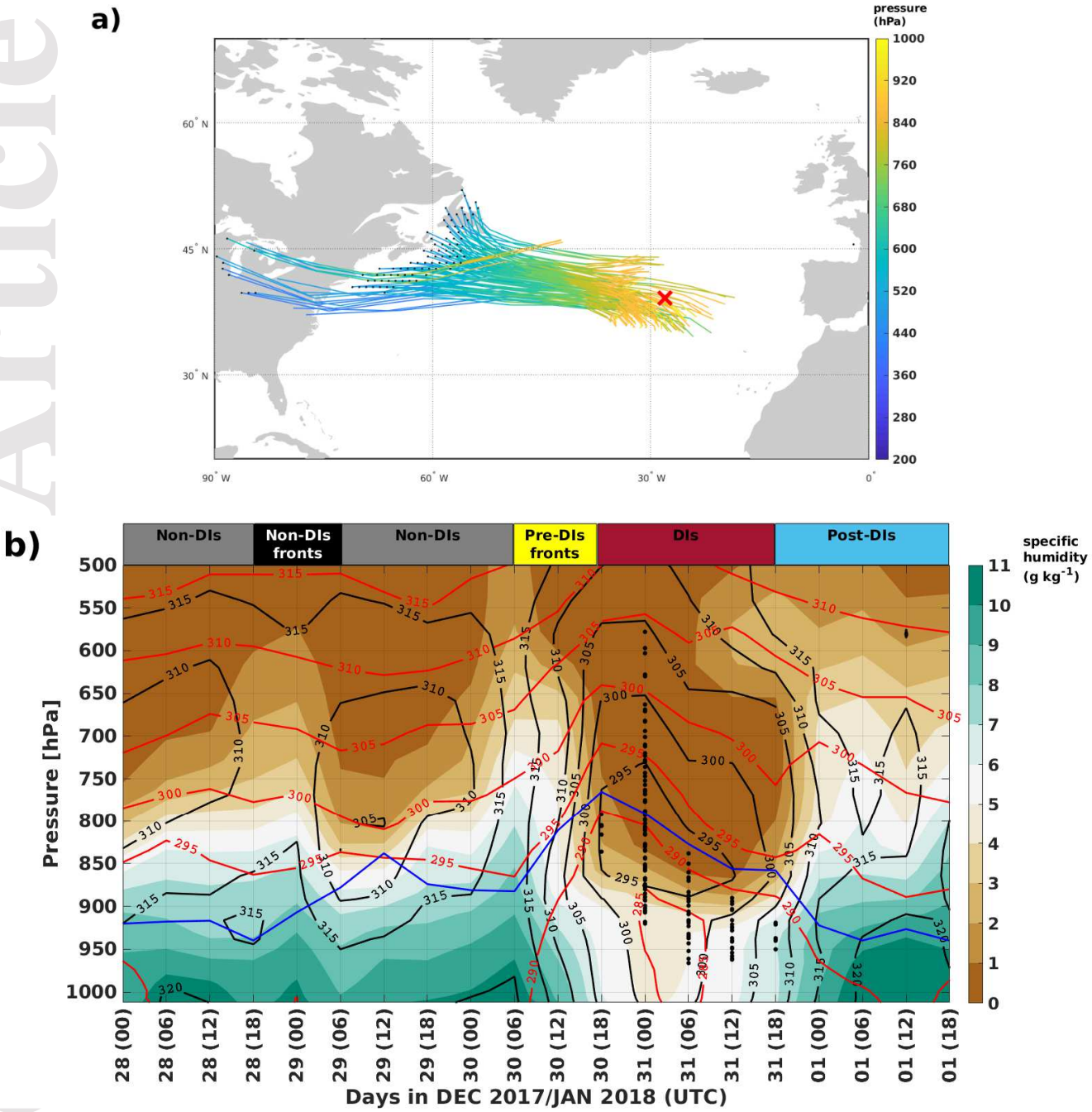

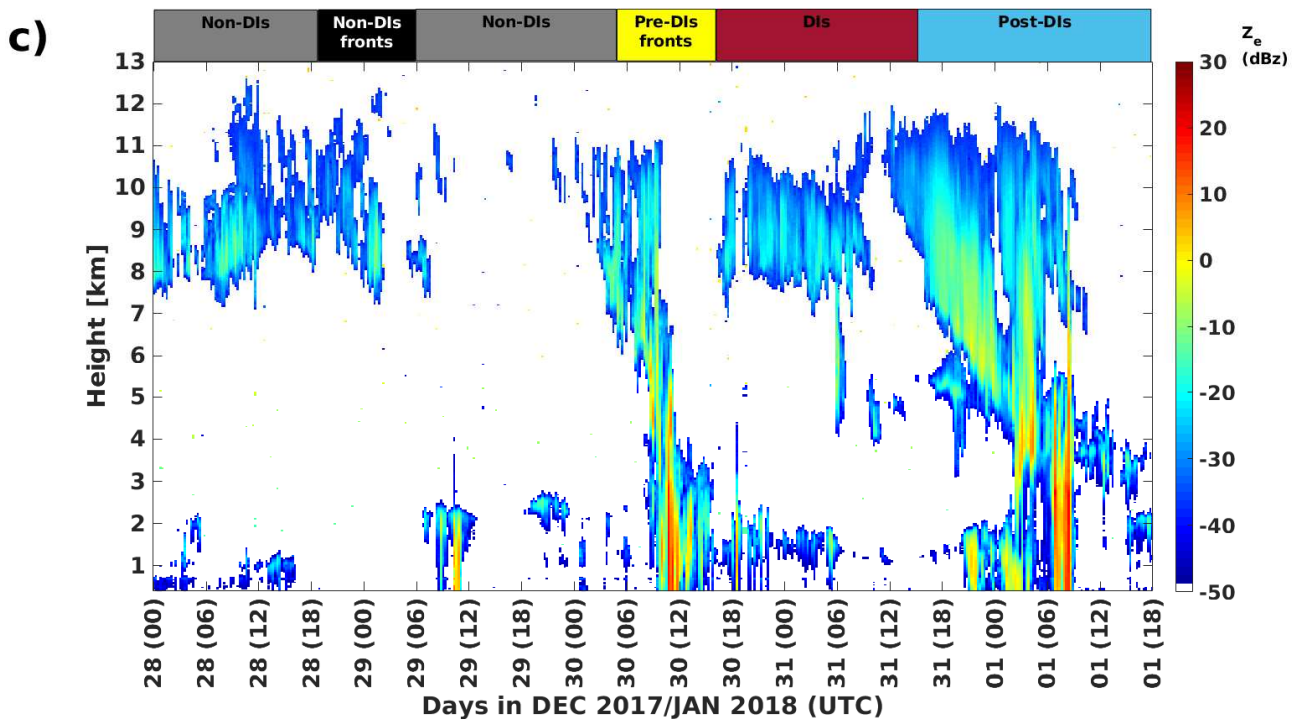

Fig. 1. A selected DI event from 28 DEC 2017 00 UTC to 01 JAN 2018 18 UTC. (a) DI trajectories starting their 48-h long descent at 12 UTC 29 DEC 2017, colored according to their pressure level (hPa). The black dots mark the location of the trajectories at initial time. The red 'x' marks the location of ENA site. (b) Time-height cross section of specific humidity ($g\ kg^{-1}$; shaded), potential temperature (K; red contours), equivalent potential temperature (K; black contours) and boundary layer height (blue line) at ENA site (39.1^{o}N,28.0^{o} W). Data are taken from ERA-I. (c) Retrieval of KAZR radar reflectivity (dBz).

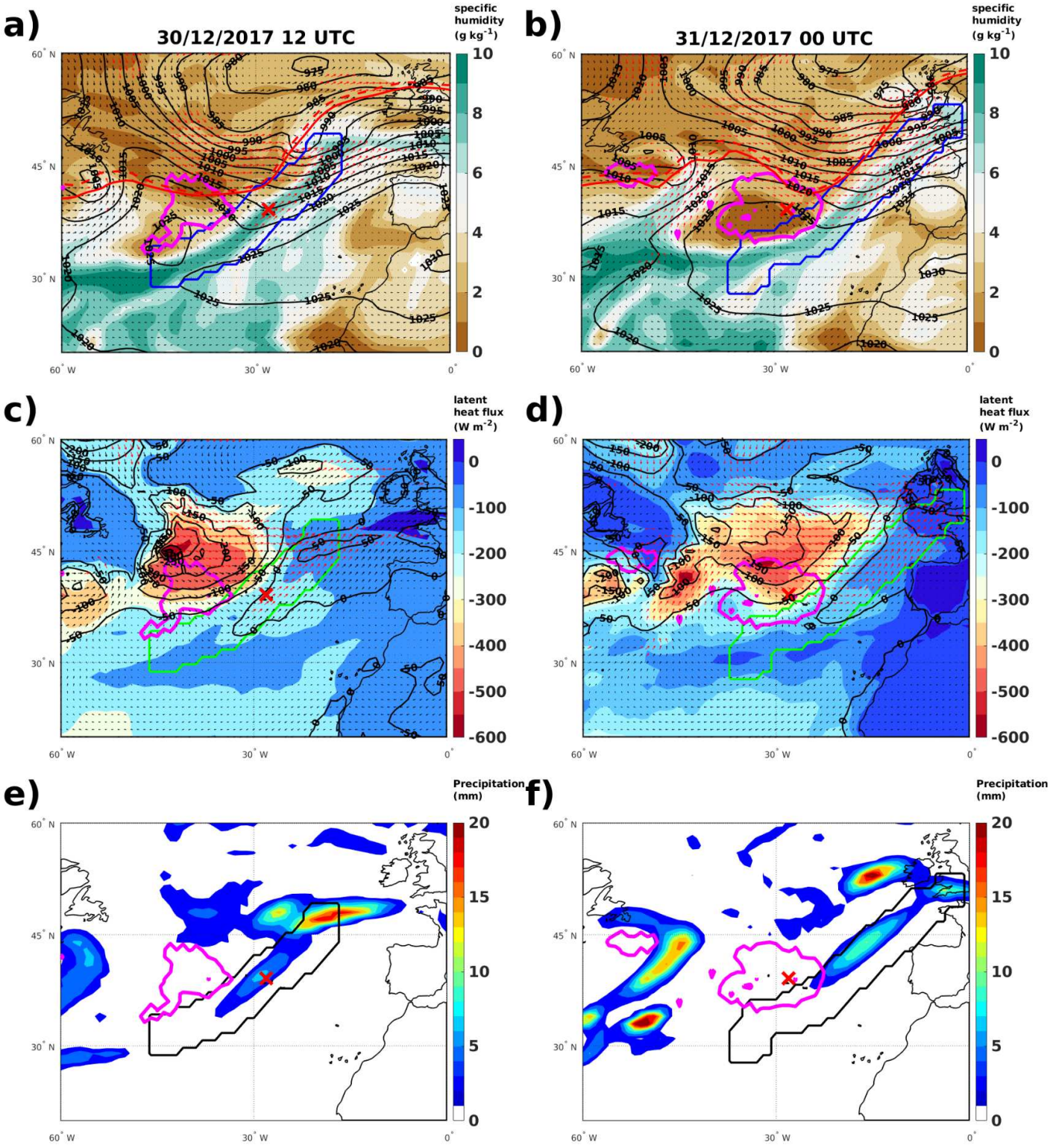

Fig. 2. Atmospheric parameters during two stages of the DI event, 12 UTC 30 December 2017 (pre-DI stage, left column) and 00 UTC 31 December 2017 (DI stage, right column). (a,b) Specific humidity ($g\ kg^{-1}$) at 850 hPa, SLP (black contours, at 5-hPa intervals), wind arrows at 850 hPa (red arrows for wind speeds exceeding 10 m s^{-1}). PV on the 315 K isentropic surface is overlaid (2 and 3 PVU in red solid and dashed contours, respectively). (c,d) Surface latent heat flux ($W\ m^{-2}$, shaded), surface sensible heat flux (black contour, at 50 $W\ m^{-2}$ intervals). Negative indicates ocean heat loss to the atmosphere. (e,f) Total accumulated precipitation over the preceding 6 h (mm). In all panels, the red 'x' marks the location of ENA site, DIs outflow is encircled by the magenta contour, and the expanded cold front region is marked by the blue (a,b), green (c,d) and black (e,f) contour.

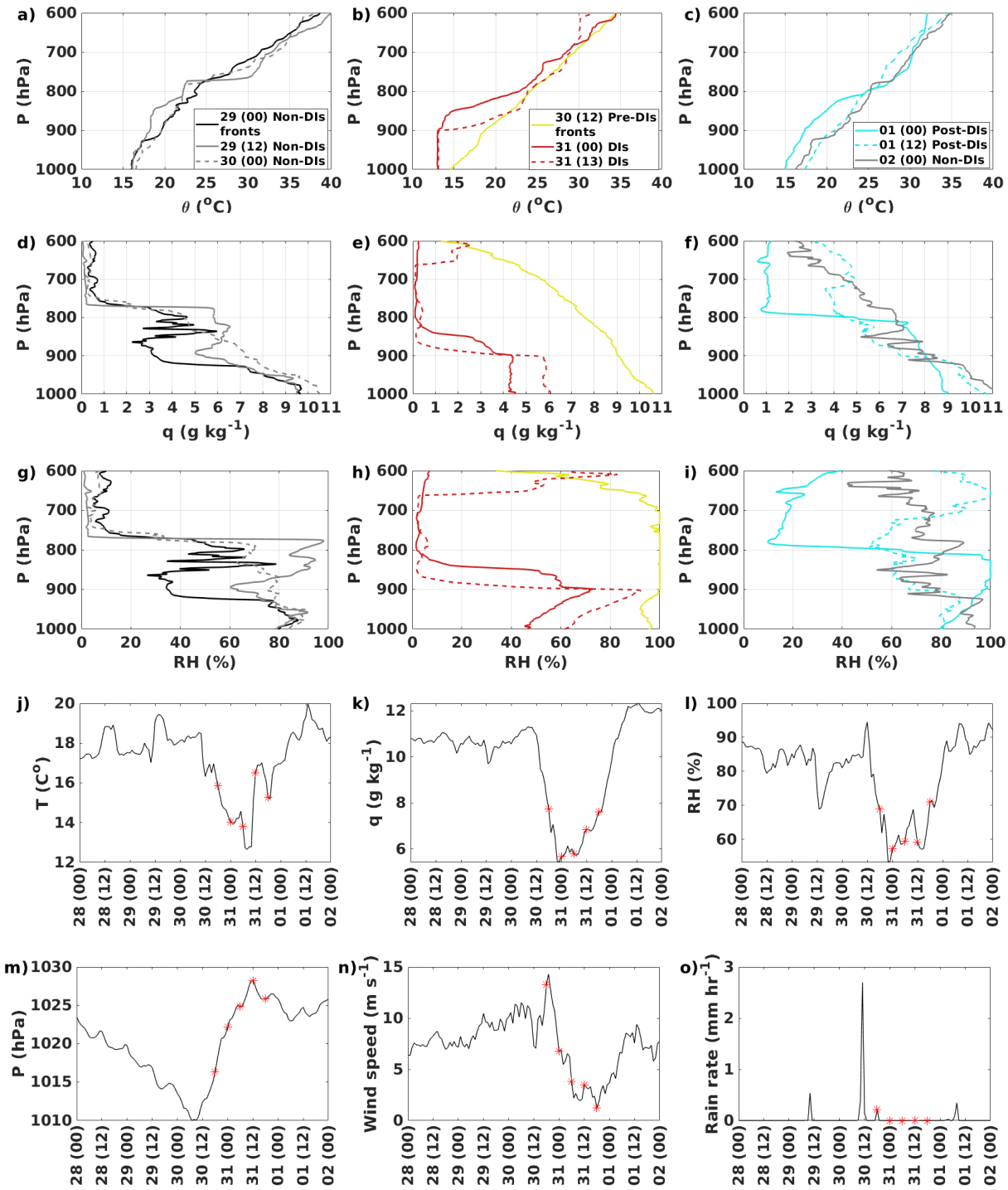

Fig. 3. Radiosondes vertical profiles of (a-c) potential temperature (℃), (d-f) water vapor mixing ratio ($g\ kg^{-1}$), and (g-i) relative humidity (%) for difference time. Hourly time evolution of **s**urface measurements: (j) temperature (℃), (k) water vapor mixing ratio ($g\ kg^{-1}$), (l) relative humidity (%), (m) pressure (hPa), (n) wind speed ($m\ s^{-1}$) and (o) rain rate ($mm\ hr^{-1}$). The red stars in (j)-(o) mark the time of DIs.

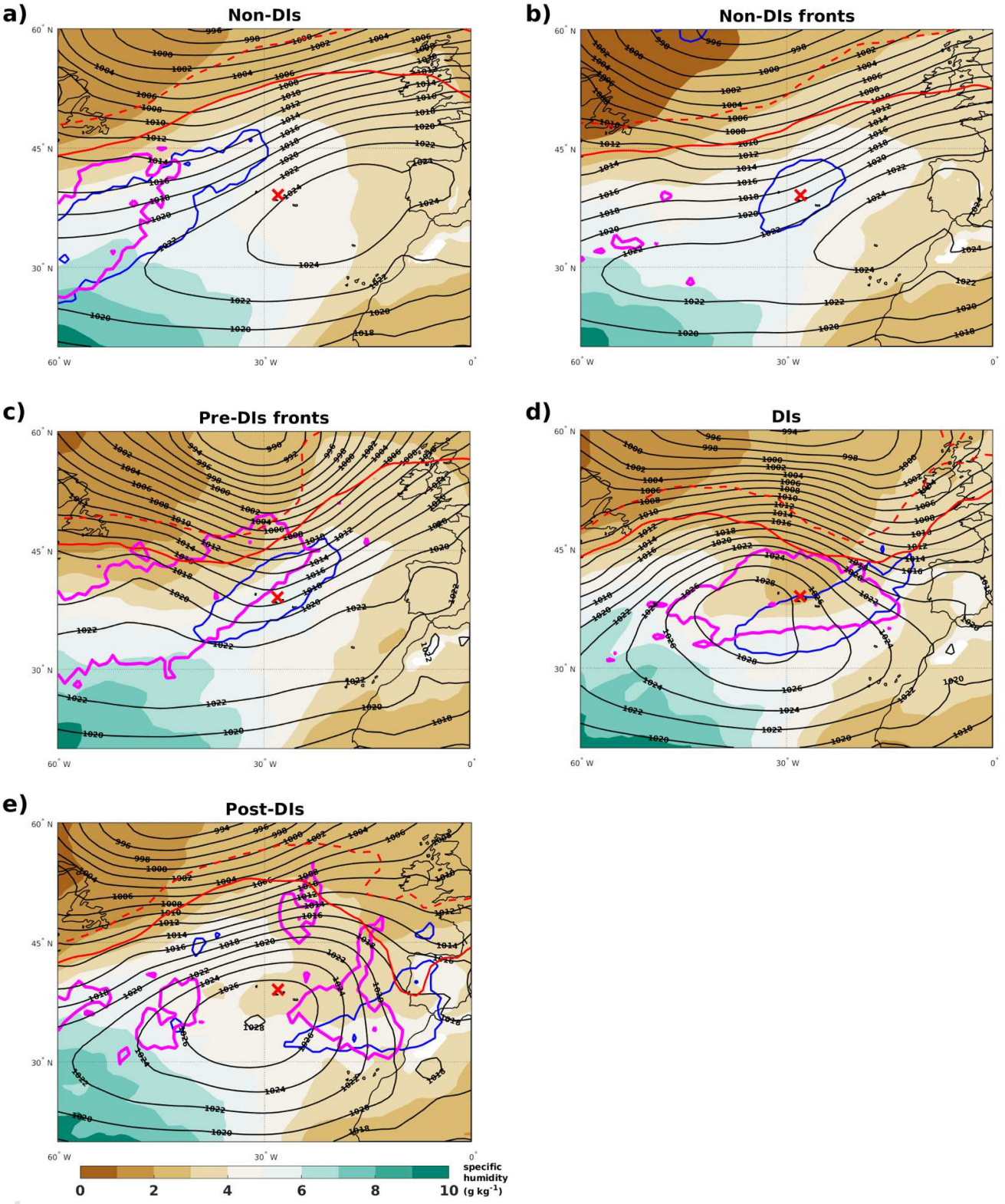

Fig. 4. Composite specific humidity ($g\ kg^{-1}$) at 850 hPa overlaid with the 2 and 3-PVU on the 315K isentropic surface (solid and dashed red contours, respectively) and SLP (black contours, at 2 hPa intervals) for all categories: (a) Non-DIs, (b) Non-DIs-fronts, (c) Pre-DIs fronts, (d) DIs, and (e) Post-DIs. In all panels, the red 'x' marks the location of ENA site, DIs outflow is encircled by the magenta contour, and the expanded cold front region is marked by the blue contour. Data are from ERA-Interim for DJF 2016-2018.

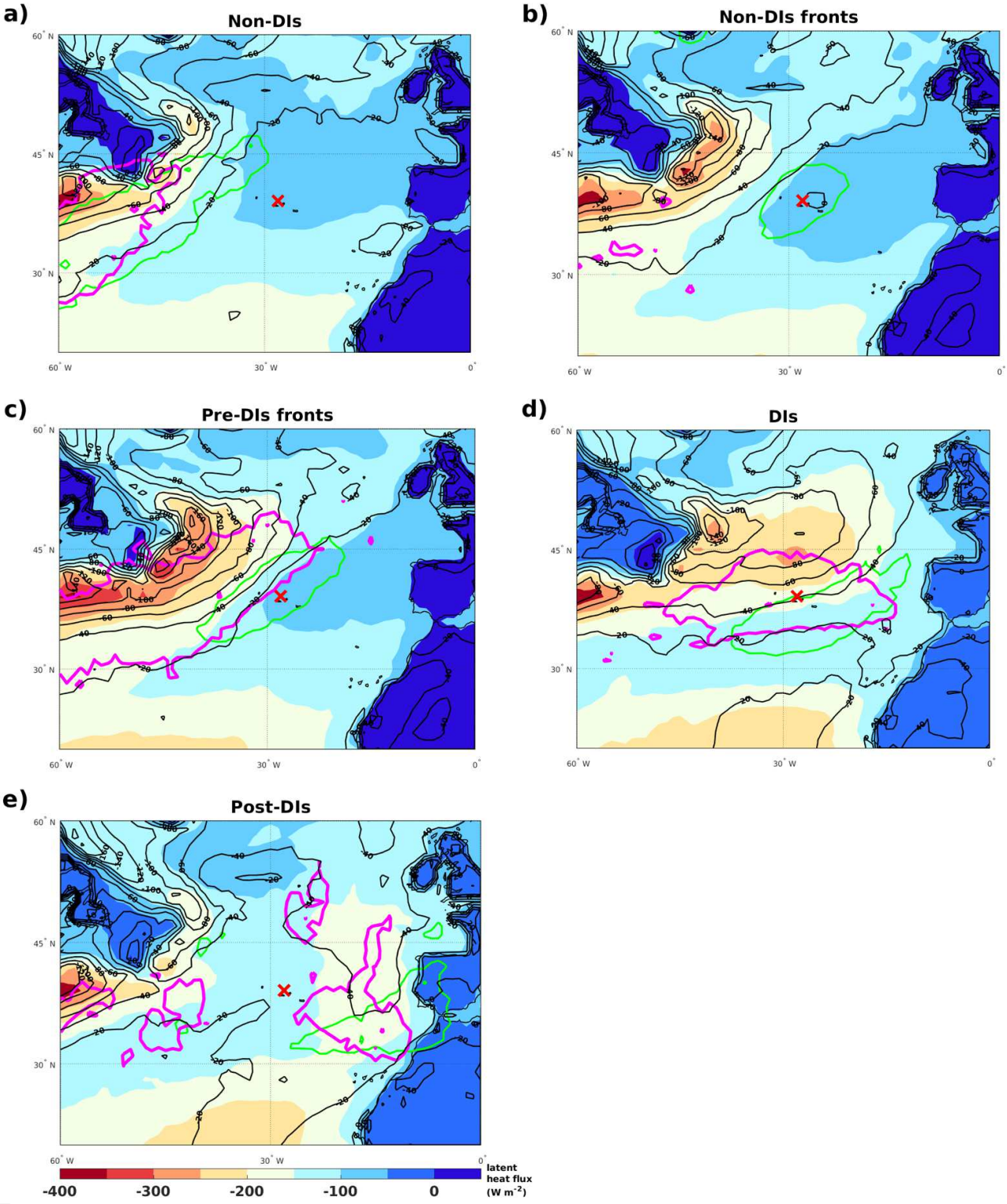

Fig. 5. Composite surface latent heat flux ($W\,m^{-2}$) overlaid with sensible heat fluxes (black contours, at 20 $W\,m^{-2}$ intervals) for all categories: (a) 'Non-DIs', (b) 'Non-DIs'-fronts, (c) Pre-DIs fronts, (d) DIs, and (e) Post-DIs. In all panels, the red 'x' marks the location of ENA site, DIs outflow is encircled by the magenta contour, and the expanded cold front region is marked by the green contour. Data are from ERA-Interim for DJF 2016-2018.

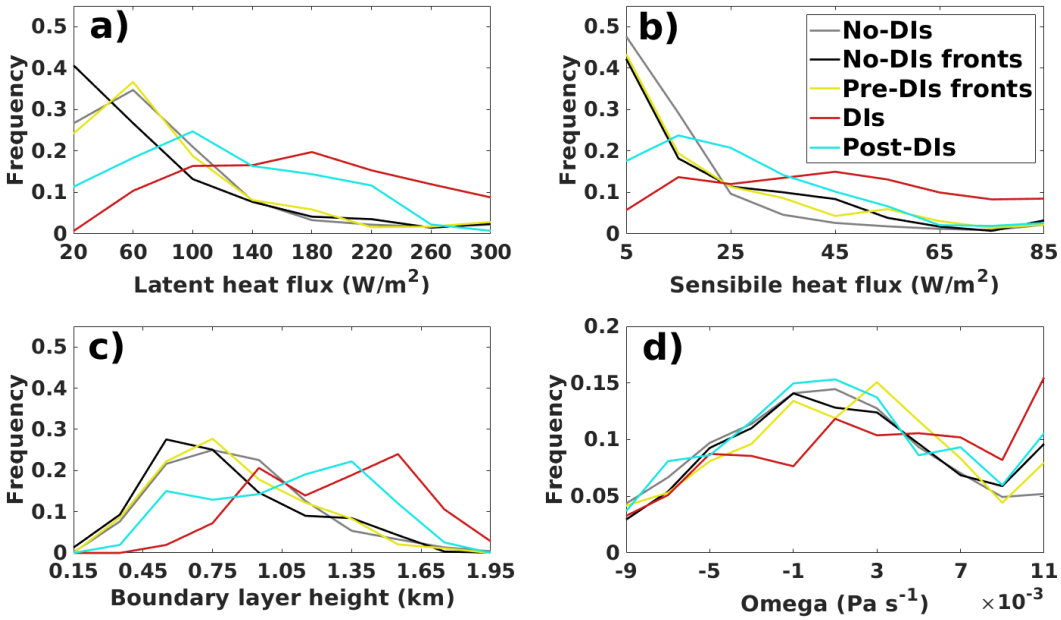

Fig. 6. Frequency distribution of (a) surface latent heat flux ($W\ m^{-2}$), (b) surface sensible heat flux ($W\ m^{-2}$), (c) boundary layer height (km) and (d) 500-hPa Omega ($Pa\ s^{-1}$) from ERA-Interim, averaged within the 9 one-degree grid points around the ENA site i.e. $38^o - 40^o$N and $29^o - 27^o$W. The frequency is normalized for each class.

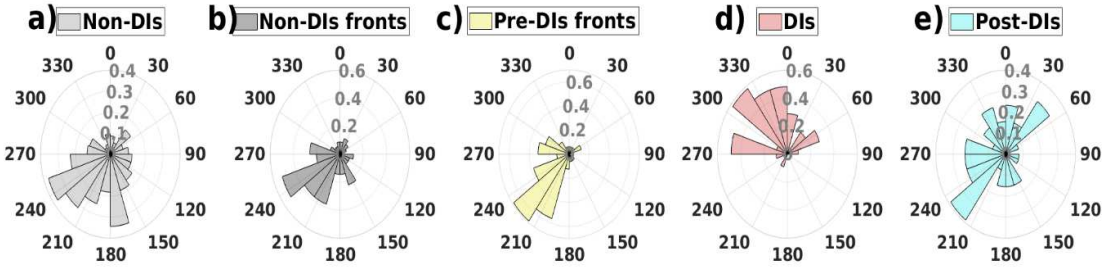

Fig. 7. Wind directions histograms from radiosondes at the lowest altitude of measurements (50 m A. G. L.) for the categories (a) Non-DIs, (b) Non-DIs fronts, (c) Pre-DIs fronts, (d) DIs, and (e) Post-DIs. Northerly wind is indicated by 0 degrees. Please note that the length of the bars in the radial direction indicates the frequency of occurrence for each direction, and not the wind magnitude.

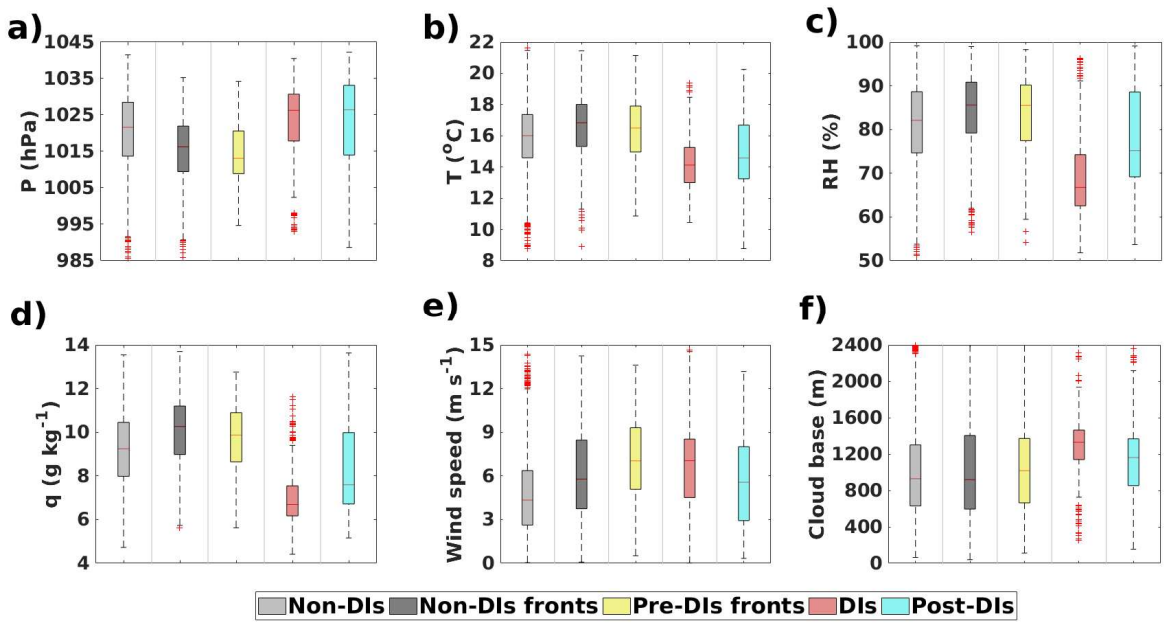

Fig. 8. Distributions of surface measurements of atmospheric parameters for the different categories: (a) Pressure, (b) temperature, (c) relative humidity, (d), water vapor mixing ratio, (e), horizontal wind speed, and (f) Cloud base height. The thick horizontal line marks the median value of distributions. The boxes correspond to 25^{th} and 75^{th} percentiles of the distributions, the whiskers to the 5th and 95th percentiles and the red crosses mark the outliers.

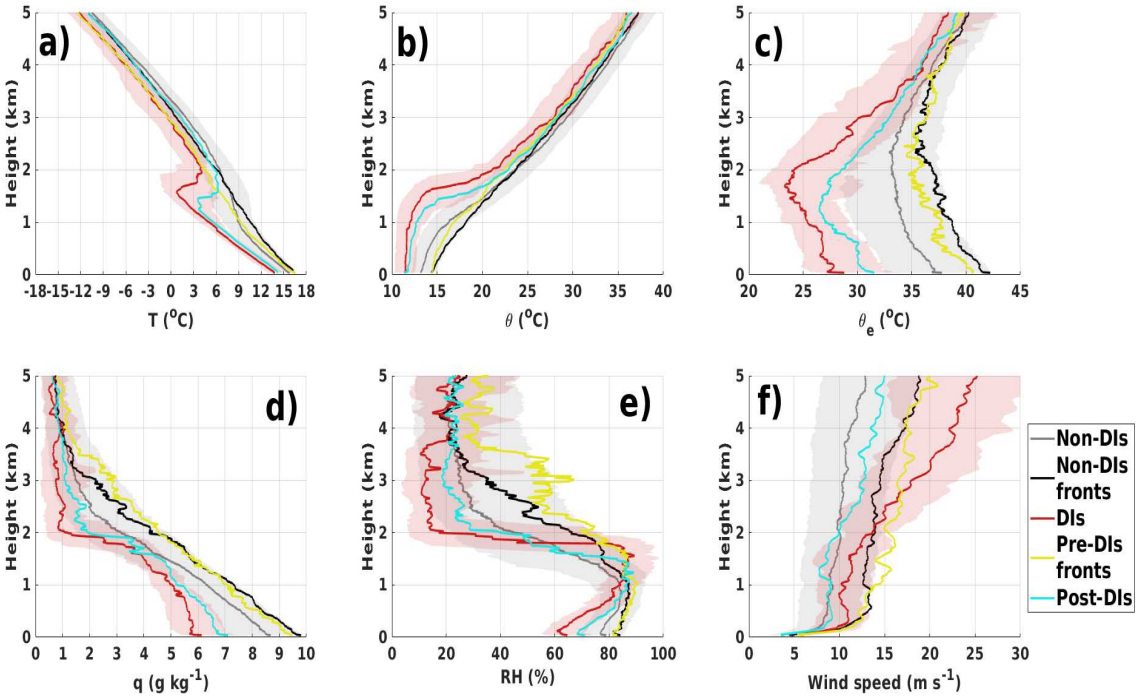

Fig. 9. Radiosondes vertical profiles of (a) air temperature, (b) potential temperature, (c) equivalent potential temperature, (d) water vapor mixing ratio, (e) relative humidity, and (f) horizontal wind speed. The solid lines are the median value at each height and category, and the shaded area marks the range between the 25^{th} and 75^{th} percentiles of the Non-DIs and DIs distributions.

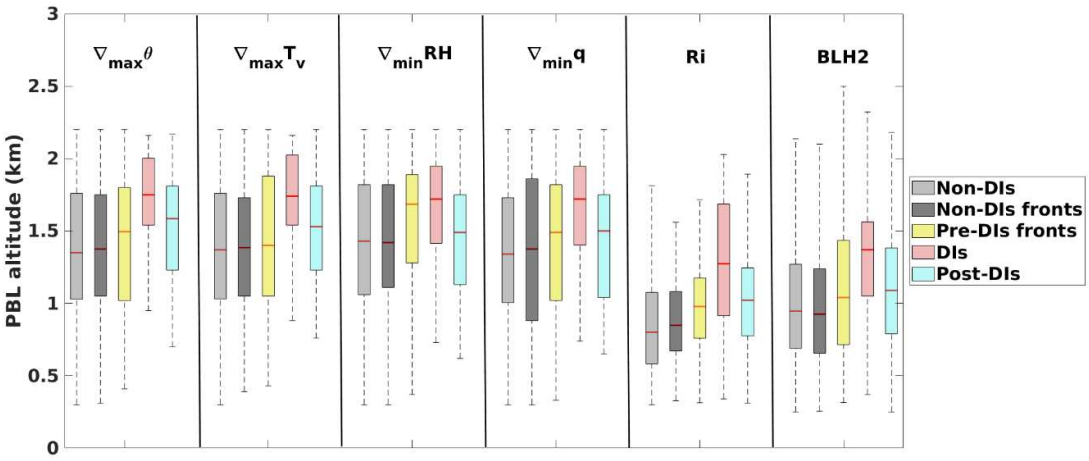

Fig. 10. PBL height (km) distributions according to six methodologies for each dynamical category. Five definitions are based on radiosondes data: Ri uses the bulk Richardson threshold of 0.25, four gradient definitions follow Von Engeln and Teixeira (2013). BLH2 is additionally derived from independent ceilometer data (see Section 2.4 for exact definitions). The boxes correspond to 25^{th} and 75^{th} percentiles of the distributions, the whiskers to the 5th and 95th percentiles and the red crosses mark the outliers.

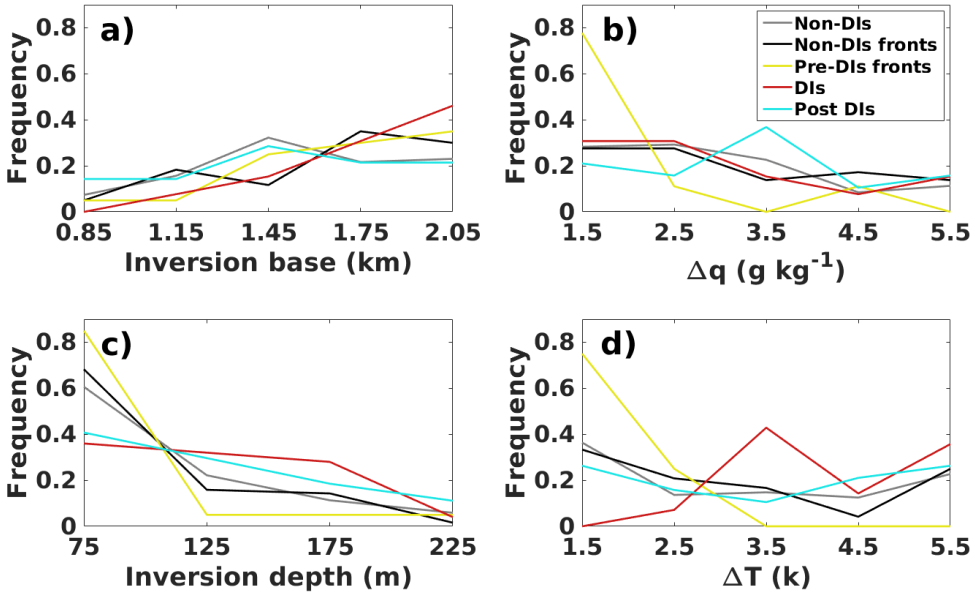

Fig. 11. Frequency distribution of (a) inversion base height (km), (b) mixing ratio difference between the bottom and top of the inversion layer (g kg^{-1}), (c) inversion depth (m), and (d) temperature difference between the top and bottom of the inversion layer (k) based on radiosondes, for all categories.

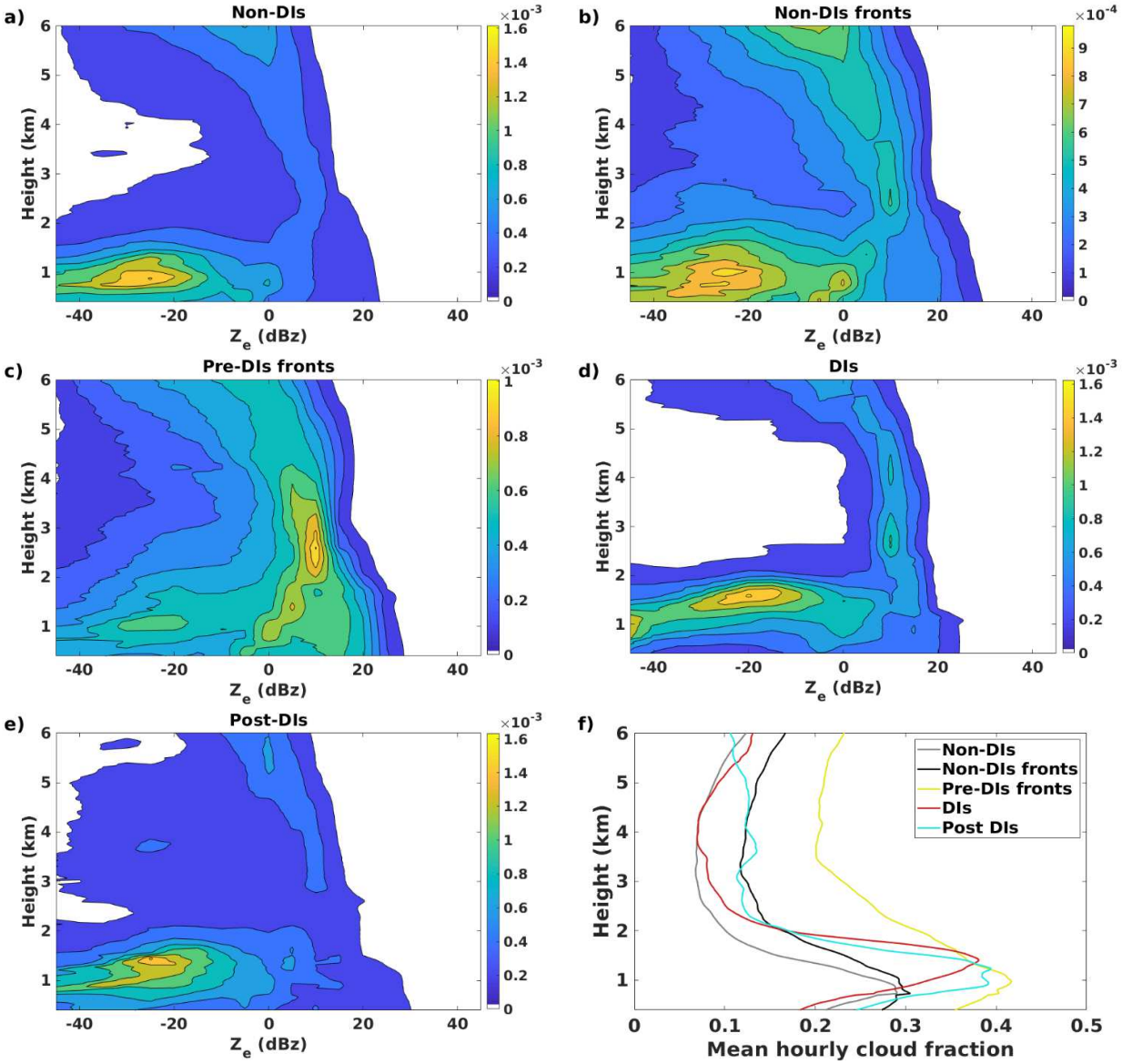

Fig. 12. The CFAD of radar reflectivity from KAZR. (a) Non-DIs, (b) Non-DIs fronts, (c) Pre-DIs fronts, (d) DIs, (e) Post-DIs. (f) Vertical profile of mean hourly cloud fraction estimated from KAZR, averaged for each dynamical class.

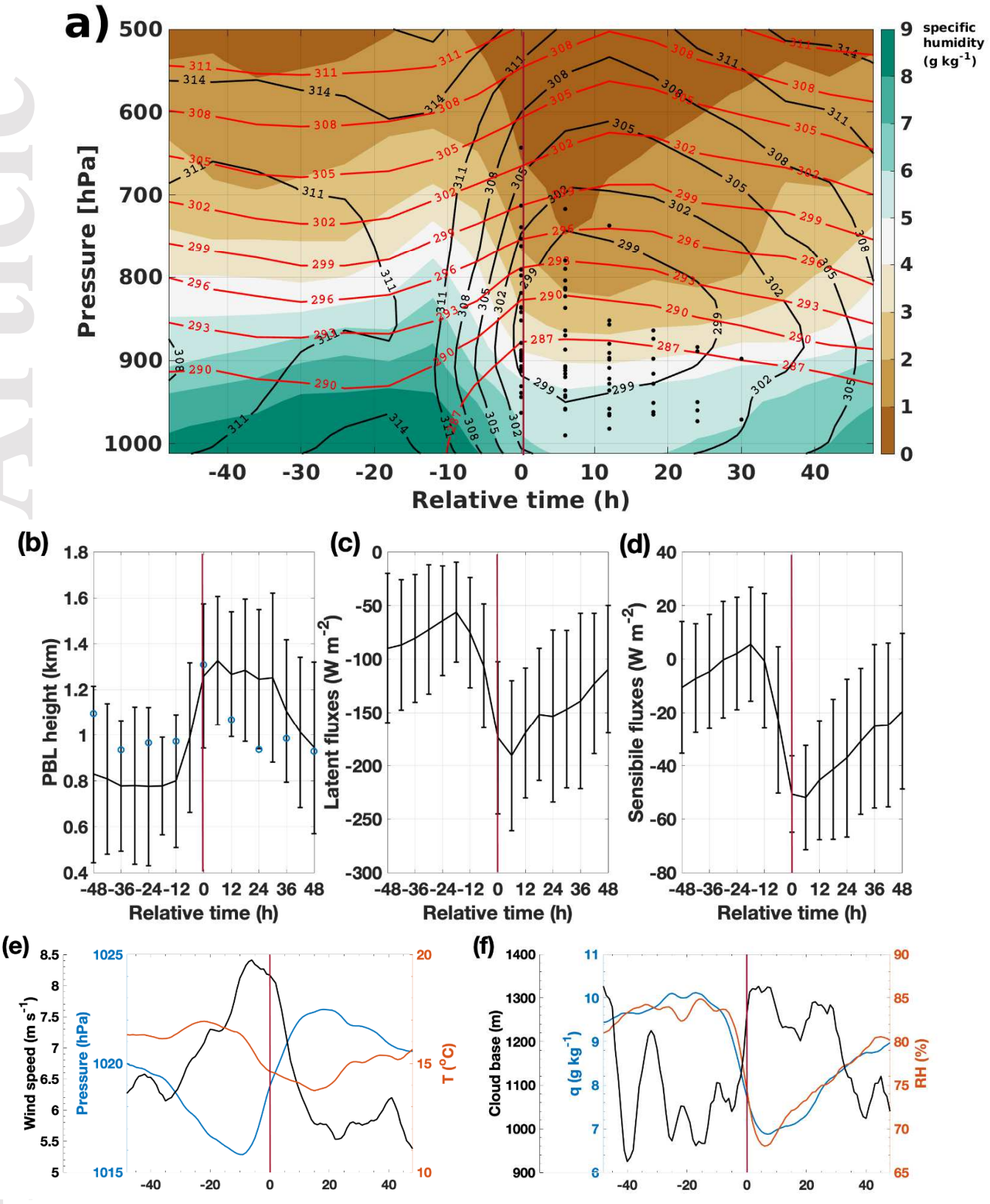

Fig. 13. Composite temporal evolution of 31 DI events. Relative time 0 h marks the initial occurrence of DIs within a 1-degree radius of ENA site (shown with a vertical red line). Shown are (a) mean time-height cross section of specific humidity (g kg^{-1}), potential temperature (K, red contours) and equivalent potential temperature (K, black contours) from ERA Interim. Also shown is the event distribution of the highest DI pressure recorded at each relative time step (black points). (b) Time series of PBL height (km) based on Bulk Richardson number of 0.25 in ERA-Interim (solid black) and ENA site radiosondes (blue points at 12-h intervals). (c) Surface latent heat fluxes and (d) surface sensible heat fluxes ($W\ m^{-2}$), from ERA-Interim data. The vertical lines in (b-d) mark the standard deviation. Time evolution of average meteorological surface measurements: (e) pressure (hPa), temperature (℃) and wind speed ($m\ s^{-1}$), (f) mixing ratio ($g\ kg^{-1}$), relative humidity (%) and cloud base height (m).

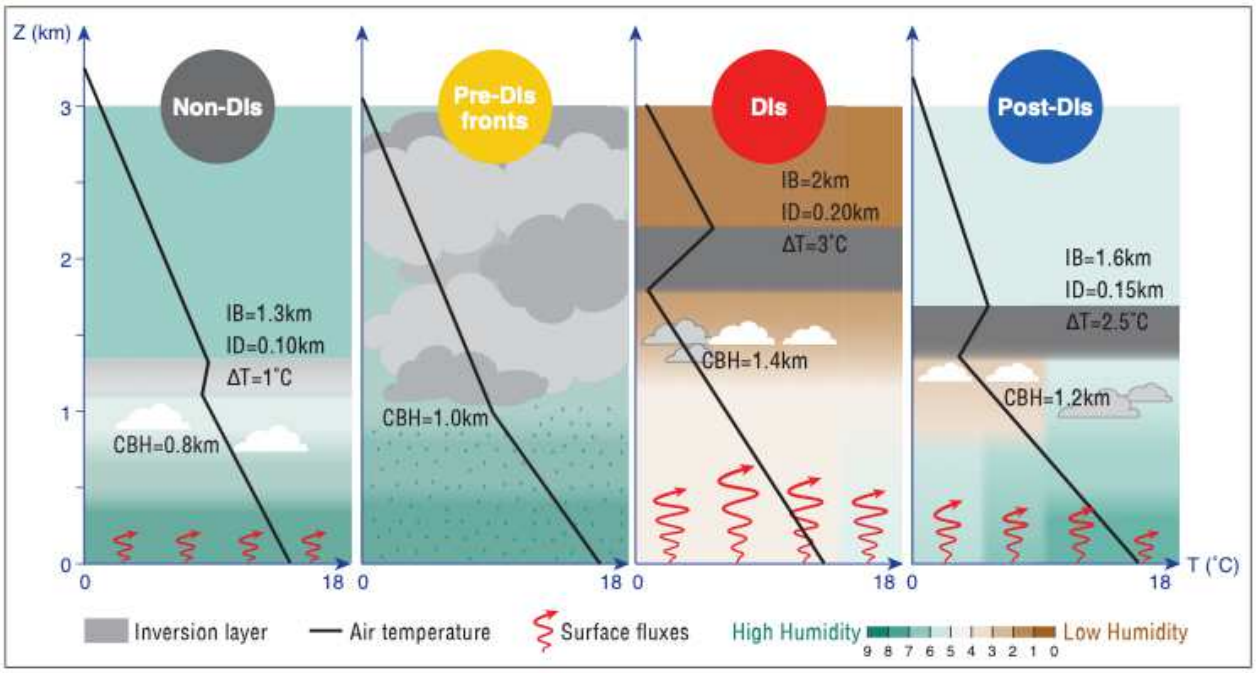

Fig. 14. Schematic summary of MBL characteristics at ENA site for each category.

REFERENCE

Aemisegger, F., & Papritz, L. (2018). A climatology of strong large-scale ocean evaporation events. Part I: Identification, global distribution, and associated climate conditions. *Journal of Climate, 31*(18), 7287-7312. https://doi.org/10.1175/JCLI-D-17-0591.1

Bony, S., Stevens, B., Frierson, D. et al. (2015). Clouds, circulation and climate sensitivity. *Nature Geoscience* 8, 261–268. https://doi.org/10.1038/ngeo2398

Bretherton, C. S., and Wyant, M. C. (1997). Moisture transport, lower tropospheric stability and decoupling of cloud-topped boundary layers. *Journal of Atmospheric Science, 54*, 148-167.

Browning, K. A. (1997). The dry intrusion perspective of extra-tropical cyclone development. *Meteorological Applications, 4*, 317-324.

Browning, K. A., & Golding, B. W. (1995). Mesoscale aspects of a dry intrusion within a vigorous cyclone. *Quarterly Journal Royal Meteorological Society., 121*, 463-493, doi:10.1002/qj.49712152302.

Browning, K. A., & Reynolds, R. (1994). Diagnostic study of a narrow cold-frontal rainband and severe winds associated with a stratospheric intrusion. *Quarterly Journal of the Royal Meteorological Society, 120*(516), 235-257.

Carlson, T. N. (1980). Airflow through midlatitude cyclones and the comma cloud pattern. *Monthly Weather Review, 108*, 1498–1509. **https://doi.org/10.1175/1520-0493(1980)108<1498:ATMCAT>2.0.CO;2**

Carr, F. H., & Millard, J. P. (1985). A composite study of comma clouds and their association with severe weather over the Great Plains. *Monthly Weather Review, 113*, 370-387, doi:10.1175/1520-0493(1985)113<0370:ACSOCC>2.0.CO;2.

Catto, J. L., & Raveh-Rubin, S. (2019). Climatology and dynamics of the link between dry intrusions and cold fronts during winter. Part I: global. climatology. *Climate. Dynamics., 53*, 1873-1892. https://doi.org/10.1007/s00382-019-04745-w

Clothiaux, E. E., Ackerman, T. P., Mace, G. G., Moran, K. P., Marchand. R. T., Miller, M. A., & Martner, B. E. (2000). Objective determination of cloud heights and radar reflectivities using a combination of active remote sensors at the ARM CART sites. *Journal of Applied Meteorology and Climatology, 39*(5), 645-665.

Dee, D. P., Uppala, S. M., Simmons, A. J., Berrisford, P., Poli, P., Kobayashi, S., Andrae, U., Balmaseda, M. A., Balsamo, G., Bauer, P., Bechtold, P., et al. (2011). The ERA-Interim reanalysis: Configuration and performance of the data assimilation system. *Quarterly Journal of the Royal Meteorological Society, 137*, 553–597.

De Szoeke, S. P., K. L. Verlinden, S. E. Yuter, & Mechem, D. B. (2016). The time scales of variability of marine low clouds. *Journal of Climate, 29*, 6463–6481. https://doi.org/10.1175/JCLI-D-15-0460.1

ECMWF. (2007). Integrated Forecasting System's documentation, Part IV: Physical processes. IFS Documentation CY31R1, ECMWF, 155 pp. [Available online at http://www.ecmwf.int/sites/default/files/elibrary/2007/9221-part-ivphysical-processes.pdf.]

Field, P. R., & Wood, R. (2007). Precipitation and cloud structure in midlatitude cyclones. *Journal of Climate, 20*(2), 233-254. doi:10.1175/JCLI3998.1.

Ghate, V. P., Cadeddu, M. P., & Wood, R. (2020). Drizzle, turbulence, and density currents below post cold frontal open cellular marine stratocumulus clouds. *Journal of Geophysical Research: Atmospheres, 125*(19), 1-16. https://doi.org/10.1029/2019JD031586

Giangrande, S. E., Wang, D., Bartholmew, M. J., Jensen, M. P., Mechem, D. B., Hardin, J. C., & Wood, R. (2019). Midlatitude oceanic cloud and precipitation properties as sampled

by the ARM Eastern North Atlantic Observatory. *Journal of Geophysical Research: Atmospheres, 124*, 4741-4760. https://doi.org/10.1029/2018JD029667

Govekar, P. D., Jakob, C., Reeder, M. J., & Haynes, J. (2011). The three-dimensional distribution of clouds around Southern Hemisphere extratropical cyclones. *Geophysical Research Letters, 38*(21), L21805. https://doi.org/10.1029/2011GL049091.

Klein, S. A. & Hartmann, D. L. (1993). The seasonal cycle of low stratiform clouds. *Journal of Climate, 6*, 1587–1606.

Kollias, P., Ieng, Jo., Borque, P., Tatarevic, A., Lamer, K., Bharadwaj, N., et al. (2014). Scanning ARM cloud radars. Part II: Data quality control and processing. *Journal of Atmospheric and Oceanic Technology, 31*(3), 583-598. https://doi.org/10.1175/JTECH-D-13-00045.1

Kollias, P., Puigdomènech Treserras, B., & Protat, A. (2019). Calibration of the 2007–2017 record of Atmospheric Radiation Measurements cloud radar observations using CloudSat. *Atmospheric Measurement Techniques*, 12, 4949–4964. https://doi.org/10.5194/amt-12-4949-2019

Kotthaus, S., O'Connor, E., Münkel, C., Charlton-Perez, C., Haeffelin, M., Gabey, A. M., & Grimmond, C. S. B. (2016). Recommendations for processing atmospheric attenuated backscatter profiles from Vaisala CL31 ceilometers. *Atmospheric Measurement Techniques, 9*, 3769– 3791. https://doi.org/10.5194/amt-9-3769-2016

Lamer, K., Naud, C. M., & Booth, J. F. (2020). Relationships between precipitation properties and large-scale conditions during subsidence at the Eastern North Atlantic observatory. *Journal of Geophysical Research: Atmospheres, 124*. https://doi.org/10.1029/2019JD031848

Lamraoui, F., Booth, J. F., Naud, C. M., Jensen, M. P., & Johnson, K. L. (2019). The interaction between boundary layer and convection schemes in a WRF simulation of Post cold frontal clouds over the ARM East North Atlantic site. *Journal of Geophysical Research: Atmosphere*, *124*, 4699-4721. https://doi.org/10.1029/2018JD029370

McCoy, I. L., Wood, R., & Fletcher, J. K. (2017). Identifying meteorological controls on open and closed mesoscale cellular convection associated with marine cold air outbreaks. *Journal of Atmospheric Science, 122*(11), 678-702. https://doi.org/10.1002/2017JD027031

Mechem, D. B., Kogen, Y. L., & Schultz, D. M. (2010). Large eddy observations of popst-cold-frontal continental stratus. *Journal of the Atmospheric Science, 67*, 3368-3383. https://doi.org/10.1175/2010JAS3389.1

Mechem, D. B., Wittman, C. S., Miller, M. A., Yuter, S. E., & de Szoeke, S. P. (2018). Joint synoptic and cloud variability over the Northeast Atlantic near the Azores. *Journal of Applied Meteorology and Climatology, 57*(6). https://doi.org/10.1175/JAMC-D-17-0211.1

Medeiros, B., Hall, A., & Stevens, B. (2005). What controls the mean depth of the PBL? *Journal of Climate, 18*, 3157-3172, doi:10.1175/JCLI3417.1.

Naud, C. M., Booth, J. F., & Lamraoui, F. (2018). Post cold frontal clouds at the ARM Eastern North Atlantic site: An examination of the relationship between large-scale environment and low-level cloud properties. *Journal of Geophysical Research: Atmospheres, 123*(12),117–132. https://doi.org/10.1029/2018JD029015

Naud, C.M., Booth, J. F., Lamer, K., Marchand, R., Protat, A. & McFarquhar, G. M. (2020). On the relationship between the marine cold air outbreak M parameter and low-level cloud heights in the midlatitudes. *Journal of Geophysical Research: Atmosphere, 125*(13). https://doi.org/10.1029/2020JD032465

Norris, J. R. (1998). Low cloud type over the ocean from surface observations. Part I: Relationship to surface meteorology and the vertical distribution of temperature and

moisture. *Journal of Climate, 11,* 369-382. https://doi.org/10.1175/1520-0442(1998)011<0369:LCTOTO>2.0.CO;2

Norris, J. R., & Klein, A. (2000). Low cloud type over the ocean from surface observations. Part III: Relationship to vertical motion and the regional synoptic environment. *Journal of Climate, 13,* 245-256. https://doi.org/10.1175/15200442(200)013<0245:LCTOTO>2.0.CO;2

Park, S., & Shin, J. (2019). Heuristic estimation of low-level cloud fraction over the globe based on a decoupling parameterization, *Atmospheric Chemistry and Physics, 19,* 5635–5660.

Raveh-Rubin, S., & Wernli, H. (2016). Large-scale wind precipitation extremes in the Mediterranean: Dynamical aspects of five selected cyclone events. *Quarterly Journal of the Royal Meteorological Society, 142,* 3097-3114, doi:10.1002/qj.2891.

Raveh-Rubin, S. (2017). Dry Intrusions: Lagrangian Climatology and Dynamical Impact on the Planerary Boundary Layer. *Journal of Climate, 30,* 6661-6682, doi:10.1175/JCLI-D-16-0782.1.

Raveh-Rubin, S., & Catto, J. L. (2019). Climatology and dynamics of the link between dry intrusions and cold fronts during winter, Part II: Front-centred perspective. *Climate, Dynamics, 53,* 1893-1909. https://doi.org/10.1007/s00382-019-04793-2

Rèmillard, J., Kollias, P., Luke, E., & Wood, R. (2012). Marine boundary layer cloud observations at the Azores. *Journal of Climate,25,* 7381-7398. doi:10.1175/JCLI-D-11-00610.1

Rèmillard, J., & Tselioudis, G. (2015). Cloud regime variability over the Azores and its application to climate model evaluation. *Journal of Climate, 28*(24), 9707-9720. https://doi.org/10.1175/JCLI-D-15-0066.1

Sandu, I. & Stevens, B. (2011). On the factors modulating the stratocumulus to cumulus transitions. *Journal of the Atmospheric Sciences, 68*(9), 1865-1881.

Seibert, P., Beyrich, F., Gryning, S. E., Joffre, S., Rasmissen, A., & Tercier, P. (2000). Review and intercomparison of operational methods for determination of the mixing height. *Atmospheric Environment, 34*(7), 1001-1027.

Sorensen, J. H., Rasmussen, A., Ellermann, T., & Lyck, E. (1998). Mesoscale influence on long-range transport – evidance from ETEX modeling and observations. *Atmospheric Environment, 32*(24), 4207-4217.

Sprenger, M., & Wernli, H. (2015). The LAGRANTO Lagrangian analysis tool – version 2.0. *Geoscientific Model Development, 8,* 2569–2586.

Stull, R. B. (1988). An introduction to boundary layer meteorology. Kluwer Academic Publishers, the Netherlands, PP. 666.

Teixeira, J., Stevens, B., Bretherton, C. S., Cederwall, R., Doyle, J. D., Golaz, J. C., Holtslag, A. A. M., Klein, S. A., Lundquist, J. K., Randall, D. A., Siebesma, A. P., & Soares, P. M. M. (2008). The parameterization of the atmospheric boundary layer: A view from just above the inversion. *Bulletin of the American Meteorological Society, 89*(4), 453-458. https://doi.org/10.1175/BAMS-89-4-453

Uccellini, L. W., Keyser, D., Brill, K. F., & Wash, C. H. (1985). The Presidents' Day cyclone of 18-19 February 1979: Indluence of upstream trough amplification and associated tropopause folding on rapid cyclogenesis. *Monthly Weather Review, 113*(6), 81-105.

Von Engeln, A., & Teixeira, J. (2013). A planetary boundary layer height climatology derived from ECMWF Re-analysis data. *Journal of Climate, 26,* 6575-6590, doi:10.1175/JCLI-D-12-00385.1.

Wall, C. J., Hartmann, D. L., & Ma, P. -L. (2017). Instantaneous linkages between clouds and large-scale meteorology over the Southern Ocean in observations and a climate model. *J. Climate, 30,* 9455-9474. https://doi.org/10.1175/JCLI-D- 17-0156.1.

Wernli, H. (1997). A Lagrangian-based analysis of extratropical cyclones. II: A detailed case-study. *Quarterly Journal of the Royal Meteorological Society, 123*, 1677-1706, doi:10.1002/qj.49712354211.

Wiegner, M., Madonna, F., Binietoglou, I., Forkel, R., Gasteiger J., Geiβ, A., Pappalardo, G., Schäfer, K., & Thomas, W. (2014). What is the benefit of ceilometers for aerosol remote sensing? An answer from EARLINET. *Atmospheric Measurement Techniques, 7*, 1979-1997. https://doi.org/10.5194/amt-7-1979-2014

Wood, R., & Bretherton, C. S. (2006). On the relationship between stratiform low cloud cover and lower tropospheric stability. *Journal of Climate, 19*, 6425-6432.

Wood, R., Wyant, M., Bretherton, C. S., Rémillard, J., Kollias, P., Fletcher, J., et al. (2015). Clouds, aerosols, and precipitation in the marine boundary layer: An ARM Mobile Facility deployment. Bulletin of the American Meteorological Society, *96*(3), 419–440. https://doi.org/10.1175/BAMS-D-13-00180.1

Yang, F., Luke, E. P., Kollias, P., Kostinski, A. B., & Vogelmann, A. M. (2018). Scaling of drizzle virga depth with cloud thickness for marine stratocumulus cloud. *Geophysical Research Letters, 45*, 3746-3753. https://doi.org/10.1029/2018GL077145

Young, M., Monk, G., & Browning, K. (1987). Interpretation of satellite imagery of a rapidly deepening cyclone. *Quarterly Journal of the Royal Meteorological Society, 113*(478), 1089-1115.

Zheng, Y., Rosenfeld, D., & Li, Z. (2018). The relationships between cloud top radiative cooling rates, surface latent heat fluxes, and cloud-base heights in marine stratocumulus. *Journal of Geophysical Research: Atmosphere, 123*(20), 11678-1690. https://doi.org/10.1029/2018JD028579.

Zheng, Y., Rosenfeld, D., & Li, Z. (2020). A more general paradigm for understanding the decoupling of stratocumulus-topped boundary layers: the importance of horizontal temperature advection. *Geophysical Research Letters, 47*(14), p.e2020GL087697. **https://doi.org/10.1029/2020GL087697**